

1 The Eurasian Arctic Ocean along the MOSAiC drift in  
2 2019–2020: An interdisciplinary perspective on properties  
3 and processes

4 Kirstin Schulz<sup>1,2,\*</sup>, Zoe Koenig<sup>3,4,5</sup>, Morven Muilwijk<sup>4</sup>, Dorothea Bauch<sup>6,7</sup>,  
5 Clara J. M. Hoppe<sup>2</sup>, Elise S. Droste<sup>2,8</sup>, Mario Hoppmann<sup>2</sup>, Emelia J.  
6 Chamberlain<sup>9,10</sup>, Georgi Laukert<sup>11,10</sup>, Tim Stanton<sup>12</sup>, Alejandra Quintanilla-  
7 Zurita<sup>2</sup>, Ilker Fer<sup>5</sup>, Céline Heuzé<sup>13</sup>, Salar Karam<sup>13</sup>, Sebastian Mieruch-Schnülle<sup>2</sup>,  
8 Till M. Baumann<sup>5,14</sup>, Myriel Vredenburg<sup>2</sup>, Sandra Tippenhauer<sup>2</sup>, Mats A.  
9 Granskog<sup>4</sup>

10 <sup>1</sup>Oden Institute for Computational Engineering and Sciences, The University of Texas at Austin,  
11 Austin, TX, United States

12 <sup>2</sup>Alfred Wegener Institute Helmholtz Centre for Polar and Marine Research, Bremerhaven,  
13 Germany

14 <sup>3</sup>UiT The Arctic University of Norway, Tromsø, Norway

15 <sup>4</sup>Norwegian Polar Institute, Fram Centre, Tromsø, Norway

16 <sup>5</sup>Geophysical Institute, University of Bergen and Bjerknes Centre for Climate Research, Bergen,  
17 Norway

18 <sup>6</sup>Leibniz-Laboratory, University of Kiel (CAU), Kiel, Germany

19 <sup>7</sup>GEOMAR Helmholtz Centre for Ocean Research, Kiel, Germany

20 <sup>8</sup>School of Environmental Sciences, University of East Anglia, Norwich, United Kingdom

21 <sup>9</sup>Scripps Institution of Oceanography, University of California, San Diego, CA, United States

22 <sup>10</sup>Woods Hole Oceanographic Institution, Woods Hole, MA, United States

23 <sup>11</sup>School of Earth Sciences, University of Bristol, Bristol, United Kingdom

24 <sup>12</sup>Oceanography Department, Naval Postgraduate School, Monterey, CA, United States

25 <sup>13</sup>Department of Earth Sciences, University of Gothenburg, Gothenburg, Sweden

26 <sup>14</sup>Institute of Marine Research, Bergen, Norway

27 **This manuscript has been submitted for publication to Elementa: Science of**  
28 **the Anthropocene after minor revisions 4/20/2024. If accepted, the final ver-**  
29 **sion of this manuscript will be available via the “Peer reviewed Publication**  
30 **DOI” link on the right-hand side of this page and will be available open-**  
31 **access on the publisher’s website. For any question, contact Kirstin Schulz.**

## 32 Abstract

33 The Multidisciplinary drifting Observatory for the Study of Arctic Climate (MO-  
34 SAiC, 2019–2020), a year-long drift with the Arctic sea ice, has provided the  
35 scientific community with an unprecedented, multidisciplinary dataset from the  
36 Eurasian Arctic Ocean, covering high atmosphere to deep ocean across all sea-  
37 sons. However, the heterogeneity of data and the superposition of spatial and  
38 temporal variability, intrinsic to a drift campaign, complicate the interpretation  
39 of observations. In this study, we compile a quality-controlled physical hydro-  
40 graphic dataset with best spatio-temporal coverage and derived core parameters,  
41 including the mixed layer depth, heat fluxes over key layers, and friction veloc-  
42 ity. We provide a comprehensive and accessible overview of the ocean conditions  
43 encountered along the MOSAiC drift, discuss their interdisciplinary implications,  
44 and compare common ocean climatologies to these new data. Our results indi-  
45 cate that, for the most part, ocean variability was dominated by regional rather  
46 than seasonal signals, carrying potentially strong implications for ocean biogeo-  
47 chemistry, ecology, sea ice, and even atmospheric conditions. Near-surface ocean  
48 properties are strongly influenced by the relative position of sampling, within or  
49 outside the river-water influenced Transpolar Drift, and seasonal warming and  
50 meltwater input. Ventilation down to the Atlantic Water layer in the Nansen Basin  
51 allows for a stronger connectivity between subsurface heat and the sea ice and  
52 surface ocean via elevated upward heat fluxes. The Yermak Plateau and Fram  
53 Strait regions are characterized by heterogeneous water mass distributions, ener-  
54 getic ocean currents, and stronger lateral gradients in surface water properties in  
55 frontal regions. Together with the presented results and core parameters, we offer  
56 context for interdisciplinary research, fostering an improved understanding of the  
57 complex, coupled Arctic System.

## 58 1. Introduction

59 To a large extent, the Arctic Ocean has been historically inaccessible due to its  
60 perennial ice cover, resulting in limited data availability, particularly during win-  
61 ter. With global warming triggering rapid transformations in the Arctic (Rantanen  
62 et al., 2022), a better understanding of processes in the Arctic Ocean and its role  
63 in the coupled climate system is urgently needed to accurately predict the effects  
64 of a changing climate. Ongoing changes in the Arctic Ocean include declining  
65 sea ice cover and longer open water seasons (e.g., Stroeve et al., 2008; Kwok,  
66 2018; Kim et al., 2023), Atlantification, i.e., the progression of conditions typi-  
67 cal for the North Atlantic further into the Arctic Ocean (Polyakov et al., 2017),

68 a weakening upper ocean stratification, enhanced vertical mixing and transport  
69 (Polyakov et al., 2020b,a; Schulz et al., 2022a), increased primary productivity  
70 (Arrigo and van Dijken, 2015), and changes in the Arctic ecosystem composition  
71 (Gordó-Vilaseca et al., 2023). These changes are primarily observed in the East-  
72 ern Arctic, while conditions in the Western Arctic exhibit less clear patterns, e.g.,  
73 no conclusive evidence of increased mixing (Dosser et al., 2021; Fine and Cole,  
74 2022), or even show opposite trends, e.g., increased stratification by freshwater  
75 accumulation in the Beaufort Gyre (Timmermans and Toole, 2023).

76 The Multidisciplinary drifting Observatory for the Study of Arctic Climate  
77 (MOSAiC) was a year-long (2019–2020) drift campaign with the aim to improve  
78 our process-level understanding of the coupled Arctic System (Rabe et al., 2022;  
79 Shupe et al., 2022; Nicolaus et al., 2022; Fong and et. al., 2023). A large number  
80 of interdisciplinary efforts in MOSAiC involve physical oceanography param-  
81 eters, such as ocean temperature and salinity or current velocity. Examples include  
82 efforts to calculate the solubility of gases, to determine the origin of water masses  
83 that transport tracers and organisms, to quantify the contribution of oceanic heat  
84 to sea ice formation and melting, or to constrain the variability in ice-nucleating  
85 particles of marine origin. In addition, the modeling community requires updated  
86 oceanic boundary conditions and core parameters for model validation (Heuzé  
87 et al., 2023b), while climatological datasets, which are often crucial components  
88 in modeling frameworks, need ground-truthing to current conditions. However,  
89 the diversity of oceanographic equipment used during MOSAiC and the resulting  
90 scattered datasets at various levels of processing and documentation hinder easy  
91 access to and utilization of these data, especially for non-physical oceanographers  
92 and scientists not involved in the field campaign. In addition, the design of MO-  
93 SAiC as a drifting platform complicates the interpretation of oceanographic mea-  
94 surements. Superimposed on the annual cycle is the regionality along the more  
95 than 3500 km long drift track across the Eurasian basin (Figure 1a, Rabe et al.,  
96 2022). These challenges might lead to an inconsistent usage and interpretation of  
97 the oceanographical data and hinder the inter-comparability of individual studies  
98 in the future.

99 In this study, we compile an accessible and quality-controlled dataset of hydro-  
100 graphic profiles at the highest possible temporal resolution along the drift and pro-  
101 vide derived core parameters (Schulz et al., 2023b), including an interactive data  
102 interface (Mieruch, 2023) in the online Ocean Data View webODV (Mieruch and  
103 Schlitzer, 2023), which can be used consistently in future disciplinary and inter-  
104 disciplinary studies. Based on this dataset, we present a comprehensive overview  
105 of ocean conditions during the MOSAiC drift, discuss their effect on the coupled

106 system and to the extent possible discriminate between spatial and temporal sig-  
107 nals. This description of the state of the Eurasian Arctic Ocean in 2019–2020 and  
108 the comparison of commonly used climatological datasets to these modern data  
109 will also aid the evaluation of ocean models.

110 The structure of this paper is as follows. In Section 2, we provide a brief  
111 overview of the methods and instrumentation used in this study (more detailed in-  
112 formation is available in the supplemental material Text S1). Section 3 describes  
113 the geography along the drift track of MOSAiC and in Section 4 we summarize  
114 the water column structure and water mass distribution. Section 5 then focuses  
115 on dynamic features, such as surface and tidal current variability and eddies. Pa-  
116 rameters related to ocean mixing, such as the vertical diffusivity and heat fluxes,  
117 are presented in Section 6. In Section 7, we compare MOSAiC results to exist-  
118 ing climatologies. In the discussion (Section 8), we contextualize the MOSAiC  
119 data by comparing them to previous findings and we discuss the implications of  
120 these results for other scientific disciplines. Finally, Section 9 summarizes the  
121 main findings and concludes the paper.

## 122 2. Methods and instrumentation

123 The MOSAiC drift started in September 2019, using the icebreaker RV *Polarstern*  
124 (Knust, 2017) as a drifting platform frozen into the Arctic sea ice, with measure-  
125 ments conducted from the same ice floe and surrounding sites during five cruise  
126 legs. On-site sampling was interrupted from May 15 to June 27, 2020, due to the  
127 unavailability of a second icebreaker during the COVID-19 pandemic to perform  
128 personnel exchange and resupply, but resumed on the same floe. At the end of  
129 July, the floe disintegrated in the marginal ice zone in Fram Strait, and after relo-  
130 cation north, a second floe was chosen close to the previous drift track to sample  
131 the freeze-up period. In the following, we briefly summarize the different datasets  
132 and methods used in this study. More details can be found in the supplemental  
133 material Text S1 and an overview of the sampling locations is found in Rabe et al.  
134 (2022).

135 We obtained water depths from three different sources: the *Polarstern*  
136 echosounder, the combined altimeter and depth readings from the deep casts of  
137 the ship-based Conductivity-Temperature-Depth (CTD) profiling system and the  
138 IBCAO v4.2 bathymetric dataset (Jakobsson et al., 2020). Drift track and speed  
139 were obtained from the *Polarstern* navigation records and complemented with  
140 data from a GPS buoy (“CO1”) that remained on the floe when sampling was in-  
141 terrupted in spring. From the drift velocity, we calculated the ice friction velocity

142  $u_*$  based on the Rossby similarity (see supplemental material Text S1), as done in  
143 Kawaguchi et al. (2022).

144 In total, a set of 2,434 vertical temperature and salinity profiles were com-  
145 piled, including data from the microstructure profiler (MSS) operated at Ocean  
146 City, i.e., a sampling site in the Central Observatory (CO) on the main floe (1,665  
147 profiles, 0–350 m; Schulz et al., 2023c), the Ocean City CTD (121 profiles, down  
148 to maximum 1000 m; Tippenhauer et al., 2023a) and the *Polarstern* CTD (134  
149 profiles, excluding those during transit; Tippenhauer et al., 2023b). During the  
150 drift interruption and on days without any MSS or CTD casts, we used profiles  
151 from the ice-tethered profilers ITP94 and ITP111 (down to 1000 m depth, 428  
152 profiles in total; Toole and Krishfield, 2016) and daily mean data at five dis-  
153 crete depths (10, 25, 50, 75, 100 m) from a CTD chain on Pacific Gyre buoy  
154 2019O4 (86 days; Hoppmann et al., 2022), all deployed near the CO at the start  
155 of the drift. Data from all instruments were converted to conservative temperature  
156  $\Theta$  ( $^{\circ}\text{C}$ ) and absolute salinity  $S_A$  ( $\text{g kg}^{-1}$ ), quality-controlled and cross-calibrated  
157 where necessary (see supplemental material Text S1). Temperature readings from  
158 the *Polarstern* thermosalinograph are excluded here, as they were found to be un-  
159 reliable (supplemental Figure S1). We recommend not using these data in future  
160 analyses.

161 We calculated the mixed layer depth, i.e., the vertical extent of the surface  
162 layer with uniform temperature, salinity, and hence density, as the first depth  
163 where the potential density anomaly  $\sigma_0$  increases by  $\Delta\sigma_0 > 0.04 \text{ kg m}^{-3}$  com-  
164 pared to the surface (4–10 m) mean value (or,  $0.06 \text{ kg m}^{-3}$  if the increase in  
165 density at the base of the mixed layer is more gradual; see supplemental material  
166 Text S1). We omit giving mixed layer depth estimates in the presence of strong  
167 upper (0–10 m) ocean stratification (i.e., when there is no classical mixed layer,  
168 conditions frequently found during melt season), or when mixed layer depth esti-  
169 mates based on different density thresholds ( $0.04$  to  $0.08 \text{ kg m}^{-3}$ ) were very vari-  
170 able (i.e., the base of the mixed layer is not well defined). Surface salinity and tem-  
171 perature were calculated as the average over 4–10 m depth (to exclude sampling  
172 points within an under-ice meltwater lens in spring for the MSS), and the corre-  
173 sponding freezing point temperature was calculated based on the TEOS-10 set of  
174 equations (McDougall and Barker, 2011). Additionally, to better identify the sur-  
175 face water composition and origin, we calculated the surface layer (0–15 m) river  
176 water fraction based on an end-member analysis using  $\delta^{18}\text{O}$  isotope and salin-  
177 ity measurements (supplemental Text S1 and Table S2 Bauch et al., 2011) and  
178 colored dissolved organic matter (CDOM, an indicator for riverine water) fluores-  
179 cence from ITP94 (legs 1–4 only; e.g., Granskog et al., 2007; Gonçalves-Araujo

180 et al., 2016; Stedmon et al., 2021). We characterized water masses and layers as  
 181 follows:

- 182 • The surface mixed layer (ML) from the surface to the base of the ML as  
 183 explained above and in the supplemental material Text S1.
- 184 • The halocline layer (HAL) from the base of the ML to  $R = \frac{\alpha\Delta\theta}{\beta\Delta S} = 0.05$ ,  
 185 where  $\alpha$  is the thermal expansion and  $\beta$  is the haline contraction coefficient,  
 186 following Bourgain and Gascard (2011).
- 187 • The Atlantic Water thermocline (THERM) from the first depth below the  
 188 halocline where the temperature exceeds 0.8 times the minimum tempera-  
 189 ture in the halocline to the first depth where the temperature exceeds 0.8  
 190 times the maximum temperature of the Atlantic Water layer, as defined in  
 191 Schulz et al. (2021).
- 192 • Arctic Atlantic Water (AAW) as the conservative temperature range  $0^\circ\text{C} <$   
 193  $\Theta < 2^\circ\text{C}$  (Korhonen et al., 2013).
- 194 • Atlantic Water (AW) with conservative temperature  $\Theta > 2^\circ\text{C}$  (Rudels et al.,  
 195 2012).
- 196 • Upper Polar Deep Water (UPDW) from the first depth when temperatures  
 197 fall below  $\Theta = 0^\circ\text{C}$ , down to  $\sigma_{0.5} = 30.444\text{ kg m}^{-3}$ , the potential density  
 198 referenced at 500 m depth (Rudels, 2009).
- 199 • Eurasian Basin Deep Water (EBDW) between  $\sigma_{0.5} = 30.444\text{ kg m}^{-3}$  and  
 200  $\sigma_1 = 37.46\text{ kg m}^{-3}$  (Smethie Jr et al., 1988).  $\sigma_1$  refers to the potential  
 201 density referenced at 1000 m depth.
- 202 • Canadian Basin Deep Water (CBDW) with the same range as EBDW, but  
 203 with  $\Theta > -0.6^\circ\text{C}$  and absolute salinity  $S_A > 35.083$  following Rudels  
 204 (2009). The salinity threshold was converted from practical salinity of  
 205 34.915 in Rudels (2009) at 1500 m depth.
- 206 • Eurasian Basin Bottom Water (EBBW) from  $\sigma_1 = 37.46\text{ kg m}^{-3}$  to the sea  
 207 floor (Smethie Jr et al., 1988).
- 208 • In the Yermak Plateau and Fram Strait regions: Arctic Intermediate Water  
 209 (AIW) in the same range as UPDW ( $\Theta = 0^\circ\text{C}$  to  $\sigma_{0.5} = 30.444\text{ kg m}^{-3}$ )  
 210 following Meyer et al. (2017b).
- 211 • In the Yermak Plateau and Fram Strait regions: Nordic Sea Deep Water  
 212 (NSDW) from  $\sigma_{0.5} = 30.444\text{ kg m}^{-3}$  to the sea floor (Meyer et al., 2017b).

213 Current velocity profiles (approximately 20–400 m depth) obtained with a  
 214 75 kHz acoustic Doppler current profiler (ADCP; Baumann et al., 2021) were  
 215 used to calculate depth-averaged surface layer (14–30 m) and tidal (whole water

216 depth) currents of different frequencies (see Meyer et al., 2017b, and supplemental  
 217 Text S1 for more details in the methodology) and to visually identify eddies.  
 218 Tidal velocities were then compared to data from the Arctic Ocean Tidal Inverse  
 219 Model AOTIM5 (Erofeeva and Egbert, 2020).

220 Turbulent mixing parameters presented here are based on the dissipation rate  
 221 of turbulent kinetic energy  $\varepsilon$ , measured with the MSS (Schulz et al., 2022b). The  
 222 value  $\varepsilon$  describes how much small (0.1–1 m) scale turbulent kinetic energy (“turbulence”)  
 223 is present to mix the water column. From  $\varepsilon$ , we calculated the depth of  
 224 the surface active mixing layer, i.e., the depth range where turbulence is elevated  
 225 due to friction at the ocean-sea ice interface ( $\varepsilon \geq 5 \times 10^{-9} \text{ W kg}^{-1}$ ). From  $\varepsilon$  and the  
 226 local stratification, we calculated the turbulent diffusivity  $K_z$  along each profile,  
 227 as described in Bouffard and Boegman (2013). This method takes into account  
 228 how  $K_z$  scales in different energetic regimes, i.e., in the presence of high or low  
 229 turbulence and strong or weak stratification. Spatio-temporal averages in different  
 230 regions or over certain vertical layers were obtained using the maximum likeli-  
 231 hood estimator (MLE; Baker and Gibson, 1987) and heat fluxes over the halo-  
 232 cline and thermocline (Section 2) were calculated following Schulz et al. (2021).  
 233 In addition, eddy-correlation-based heat fluxes at 3 m depth were measured with  
 234 an Autonomous Ocean Flux buoy at a distance of 15–25 km from *Polarstern* (see  
 235 supplemental material Text S1 for details).

236 We compare four typical Arctic Ocean climatological datasets and two com-  
 237 monly used state estimates (i.e., models constrained with observational data to  
 238 minimize the misfit to these observations), listed in Table 1, to the MOSAiC data.  
 239 These data products cover different time periods, contain different types of data  
 240 from various sources and are produced using distinct methods and interpolation  
 241 procedures (see supplemental material Text S1 for details).

**Table 1. Climatologies and state estimates (*italics*) of temperature and salinity used for comparison with the MOSAiC observations (Section 7).**

<b>Dataset</b>	<b>Reference</b>	<b>Vertical layers</b>	<b>Temporal coverage</b>
PHC3	Steele et al. (2001)	24	1948–1997
WOA18	Locarnini et al. (2018); Zweng et al. (2018)	57	1955–2017
MIMOC	Schmidtke et al. (2013)	81	1970–2011
WOA23	Boyer et al. (2018)	57	1991–2020
<i>ASTE</i>	Nguyen et al. (2021)	50	2002–2017
<i>ECCOv4</i>	Forget et al. (2015)	50	1992–2015

### 242 3. Geography along the drift track

243 The Arctic Ocean is a semi-enclosed basin, connected to the Atlantic Ocean via  
244 Fram Strait between Svalbard and Greenland and the Barents Sea and to the Pa-  
245 cific via the Bering Strait between Russia and Alaska. Surrounded by wide shelf  
246 seas, the deep Arctic basin is separated by the Lomonosov Ridge, which reaches  
247 from the Siberian shelf to the Canadian shelf, into the Amerasian and Eurasian  
248 basins. The Eurasian Basin is further divided into the Amundsen Basin and the  
249 Nansen Basin by the Gakkel Ridge (Figure 1a). The shallow Yermak Plateau ex-  
250 tends northwards from the continental shelf on which the Svalbard archipelago is  
251 located, with the Nansen Basin on its eastern side and Fram Strait on its western  
252 side. These geographic divides have a large impact on Arctic Ocean circulation  
253 patterns and hence on the water column structure in the different regions. When  
254 interpreting the results from a drift campaign such as MOSAiC, regional gradients  
255 have to be taken into account.

256 The MOSAiC drift started in October 2019 in the 4400 m deep Amundsen  
257 Basin (green dot in Figure 1) and progressed parallel to the Gakkel Ridge within  
258 the basin over virtually flat bottom topography for around 5 months. The drift  
259 then crossed the rough topography of the Gakkel Ridge over a 3 week time period  
260 between March 18 and April 9, 2020 (yellow to red dot in Figure 1) and crossed  
261 the Nansen Basin. At the beginning of June, the drift reached the shallow Yermak  
262 Plateau (local depth approximately 800m, purple dot in Figure 1) northwest of  
263 Svalbard. After crossing the plateau from east to west, the floe entered the deeper  
264 waters and complex topography of Fram Strait on July 16 (blue dot in Figure 1)  
265 and drifted south, until the floe eventually broke up in the marginal ice zone.  
266 After a relocation closer to the North Pole, in the vicinity of the previous drift  
267 track (white triangle in Figure 1), measurements were resumed on a second floe  
268 in the Amundsen Basin. This time, the drift was directed northwards, parallel to  
269 the Lomonosov Ridge, until the expedition ended on September 20, 2020.

270 Compared to the water depth measurements from MOSAiC, we found that the  
271 bathymetric data from IBCAO v4.2 perform well in the basins and for the Gakkel  
272 Ridge and Yermak Plateau region, but agree less well with the highly variable  
273 bottom depth in Fram Strait. In the following, we use the bathymetric data from  
274 IBCAO and any basin averages (e.g., of temperature and salinity profiles) refer to  
275 averages over the regions indicated above and in Figure 1b, with a discrimination  
276 between conditions in the Amundsen Basin during winter (first part of the drift)  
277 and during summer (last part of the drift).



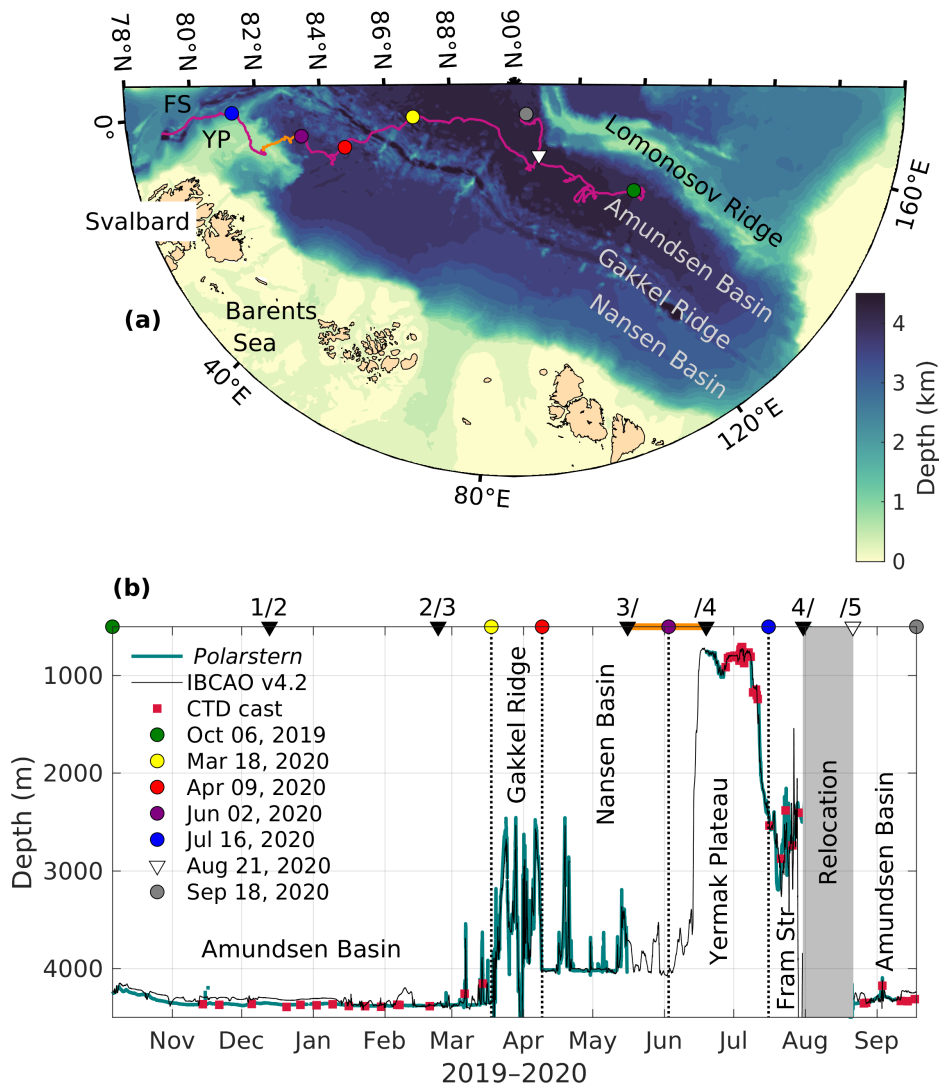


**Figure 1. Bathymetry along the drift track.**

(a) Bathymetric map of the Arctic Ocean with drift track (violet from *Polarstern*, orange from positioning buoy "CO1" between legs 3 and 4) indicated; (b) bathymetry along the drift track from the *Polarstern* echosounder (teal), International Bathymetric Chart of the Arctic Ocean (IBCAO v4.2) data set (black) and the deep conductivity, temperature, depth (CTD) casts (red squares). For better orientation, landmarks of the drift and the start and end of the individual legs are indicated with colored dots and triangles in both panels. The orange line in (b) indicates the time period when the floe was left uncrewed.

## 278 4. Water column structure and variability

279 In the following Sections, we provide a short general overview of the water masses  
280 of the Eurasian Arctic Ocean and their formation and characteristics (Section 4.1).  
281 We then elaborate on the observed variability of the near-surface waters (Sec-  
282 tion 4.2), the Atlantic Water layer (4.3) and the deep water masses (Section 4.4)  
283 during the MOSAiC drift.

### 284 4.1. *Water masses in the Arctic Ocean*

285 Large amounts of terrestrial freshwater (and other material) enter the Arctic Ocean  
286 from Siberia and are advected towards Fram Strait together with sea ice formed  
287 on the Siberian shelves transported via the Transpolar Drift (e.g., Rudels et al.,  
288 2012; Charette et al., 2020; Mysak, 2001; Karcher et al., 2012). Both the trans-  
289 port of fresh water and sea ice across the Arctic Ocean are often referred to as  
290 the "Transpolar Drift". While both transport patterns are qualitatively similar, it  
291 should be kept in mind that the exact transport pathway and the velocity of sea ice  
292 and river water-rich surface water differ (see Section 5). In this study, Transpolar  
293 Drift refers to the transport of relatively fresh, river water-rich surface water from  
294 Siberian regions towards Fram Strait unless specified otherwise.

295 The surface waters within the Transpolar Drift are characterized by high  
296 concentrations of dissolved organic carbon (DOC) and various lithogenic ele-  
297 ments and may carry organisms originating from the coastal and shelf zones  
298 (Krumpfen et al., 2019; Charette et al., 2020). Paffrath et al. (2021) showed, based  
299 on lithogenic provenance tracers, that most of the freshwater encountered in the  
300 Eurasian Arctic Ocean is derived from the Lena, Yenisei and Ob rivers, whose  
301 contributions do not fully mix and form distinct freshwater domains within the  
302 Transpolar Drift. The high nutrient load in these terrestrial waters is, in parts, al-  
303 ready utilized on the wide Siberian shelves (Laukert et al., 2022) and their role for  
304 primary production at the pan-Arctic scale is still not entirely clear (Fouest et al.,  
305 2013; Terhaar et al., 2021; Gibson et al., 2022). Mixed with ambient waters, this  
306 land-runoff forms a relatively fresh surface layer uniform in temperature and salin-  
307 ity: the polar mixed layer (ML, gray in Figure 2c). This surface layer is bound by  
308 a pycnocline, i.e., a sharp increase in density, primarily set by salinity here, over a  
309 few meters, that we refer to as the base of the surface mixed layer. Below, salinity  
310 further increases, but more gradually, i.e., over tens of meters, with temperatures  
311 at or close to the freezing point. This layer is called the Arctic halocline (teal in  
312 Figure 2c, Rudels et al. (2012); Schauer et al. (1997)). In temperature and salinity  
313 space (i.e., TS-diagrams), the halocline appears as an increase in salinity close to

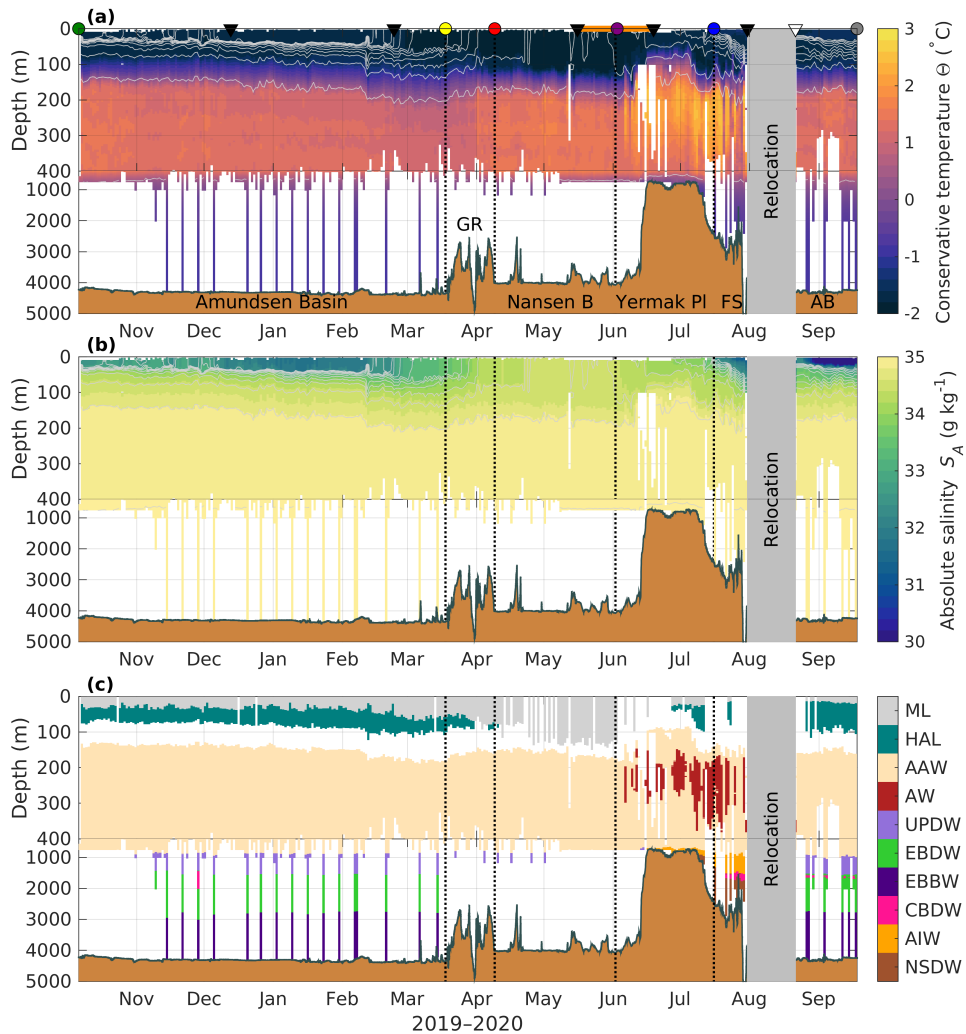


**Figure 2. Water mass distribution along the drift.**

(a) Conservative temperature ( $^{\circ}\text{C}$ ), (b) absolute salinity ( $\text{g kg}^{-1}$ ) and (c) water mass distribution along the drift, based on the composite dataset presented in this study. In (a–c), topographic regions are shown (in brown), including the Amundsen Basin (AB), Gakkel Ridge (GR), Nansen Basin (B), Yermak Plateau (PI) and Fram Strait (FS), the white regions have no data coverage. Gray lines in (a) and (b) indicate isopycnals with a spacing of  $0.2 \text{ kg m}^{-3}$ . The color bar in (c) indicates the mixed layer (ML), halocline (HAL), Arctic Atlantic Water (AAW), Atlantic Water (AW), Upper Polar Deep Water (UPDW), Eurasian Basin Deep Water (EBDW), Eurasian Basin Bottom Water (EBBW), Canadian Basin Deep Water (CBDW), Arctic Intermediate Water (AIW) and Nordic Sea Deep Water (NSDW). Data gaps in June are caused by ice-tethered profiler (ITP) data not covering the whole water column. Note that the y-axis is nonlinear, zoomed in the upper 400 m. In (a), triangles indicate the start and end of the legs, dots and vertical dotted lines the geographical markers and the orange line the uncrewed period of the drift as in Figure 1b.

314 the freezing point line (Figure 3a). Due to its strong stratification, the halocline  
315 suppresses the vertical exchange between the surface layer and underlying waters  
316 (Schulz et al., 2023a) and prevents both heat and nutrients from the Atlantic Water  
317 layer to reach the surface. In addition, the strong stratification also decouples the  
318 speed and even direction of lateral advection in the surface layer and halocline,  
319 which may all contribute to a heterogeneous distribution of tracers as well as mi-  
320 croorganisms in these layers, despite being both located in the potentially sun-lit  
321 upper ocean.

322 Relatively warm and saline water from the Atlantic enters the Arctic Ocean  
323 through eastern Fram Strait and the shallow Barents Sea, carrying high nutri-  
324 ent concentrations (Torres-Valdés et al., 2013) and organisms of Atlantic origin  
325 (Snoeijs-Leijonmalm et al., 2022). This water circulates counterclockwise along  
326 the Arctic continental slopes (Schauer et al., 1997; Rudels et al., 2012) and is  
327 modified on its pathway by heat loss to the atmosphere when it resides close to  
328 the surface in the Barents Sea (Smedsrud et al., 2013; Meyer et al., 2017a) and  
329 subsequently by mixing with colder water masses (Lenn et al., 2009; Rippeth  
330 et al., 2015). This modification appears as a temperature decrease and a progres-  
331 sively deeper position of the warm and saline Atlantic Water within the water  
332 column along its advective pathway (e.g., Schulz et al., 2021). When Atlantic  
333 Water temperatures are below 2°C, we refer to it as modified, or Arctic Atlantic  
334 Water (AAW, beige in Figure 2c). In TS-diagrams, this layer is visible as a tem-  
335 perature peak, i.e., an increase and decrease of temperature over a narrow salinity  
336 range (Figure 3a). The distribution and modification of Atlantic Water can also be  
337 inferred from provenance tracers (e.g., Bauch et al., 2016; Laukert et al., 2017,  
338 2019).

339 The identification of deep waters below the Atlantic Water layer is less  
340 straightforward, as changes in temperature and salinity at these depths can be  
341 close to the instrument precision (red box in Figure 3). Moreover, historical defi-  
342 nitions for these deep waters might not hold anymore, as the properties of the wa-  
343 ter masses involved in their formation have been changing due to ongoing global  
344 warming (Somavilla et al., 2013; von Appen et al., 2015; Karam et al., 2024).  
345 Here, we use a set of historical definitions that differ between the central basins  
346 and the regions of Yermak Plateau and Fram Strait (see Section 2), but we advise  
347 treating these results with caution. In the central Eurasian Arctic Ocean (Amund-  
348 sen and Nansen Basins), Upper Polar Deep Water (UPDW, lilac in Figure 2c)  
349 resides below the Atlantic Water layer. UPDW is a heterogeneous water mass  
350 formed as a mixture of intermediate waters flowing into the Arctic Ocean through  
351 Fram Strait and Atlantic Water, which has been strongly cooled during winter in

352 the Barents Sea, as well as saline and dense plumes formed on the shelves by  
353 brine rejection during sea ice formation (e.g., Rudels, 2009). In the TS-diagram,  
354 this water mass is a mostly straight line with increasing salinity and decreasing  
355 temperature (Figure 3b). Below the UPDW, the primary water mass is Eurasian  
356 Basin Deep Water (EBDW, green in Figure 2c), with occasional intrusions of rel-  
357 atively warm and saline Canada Basin Deep Water (CBDW, pink in Figure 2c).  
358 EBDW is characterized by nearly constant temperature and is the result of the  
359 interaction between inflowing deep waters through Fram Strait and dense plumes  
360 from the shelves (e.g., Smethie Jr et al., 1988). CBDW enters the Eurasian Basin  
361 across the Lomonosov Ridge and proceeds as a narrow boundary current, but is  
362 episodically transported into the interior basin by eddies (Karam et al., 2023). The  
363 water mass close to the sea floor is called Eurasian Basin Bottom Water (EBBW,  
364 dark purple in Figure 2c), whose properties are impacted notably by dense over-  
365 flows and geothermal heating (e.g., Smethie Jr et al., 1988). In Fram Strait, there  
366 is Arctic Intermediate Water (AIW, orange in Figure 2c) instead of UPDW be-  
367 low the Atlantic Water layer and Norwegian Sea Deep Water (NSDW, brown in  
368 Figure 2c) closer to the sea floor. AIW is characterized by nearly constant salin-  
369 ity and decreasing temperatures with depth and is typically enriched in oxygen,  
370 as it is formed through open ocean convection in the Nordic Seas (e.g., Meyer  
371 et al., 2017b). NSDW used to be seen as a cold, fresh and very dense water mass  
372 but has warmed rapidly since the cessation of Nordic Seas deep convection, as  
373 it is no longer replenished. It now closely resembles EBDW (von Appen et al.,  
374 2015; Karam et al., 2023). All the deep water masses are different mixtures be-  
375 tween water of Atlantic origin and waters entrained by deep convection (NSDW)  
376 or dense water overflows (all Eurasian basins deep waters) and therefore have  
377 different tracer properties, especially oxygen (Karam et al., 2023) and transient  
378 tracers (Heuzé et al., 2023a).

#### 379 4.2. *Surface and subsurface layer properties along the MOSAiC* 380 *drift*

381 The Amundsen Basin in early winter is characterized by a well-defined surface  
382 mixed layer close to the freezing point down to around 30 m depth and a stable  
383 halocline below (Figure 4a,d). Intermediate surface salinities around  $33 \text{ g kg}^{-1}$   
384 combined with low CDOM concentrations (Figure 4b,c) suggest that the contri-  
385 bution of river water is relatively small here. This could be related to different  
386 freshwater sources and their respective advective pathways, as the distribution  
387 of neodymium isotopes indicates alternating freshwater domains in this region

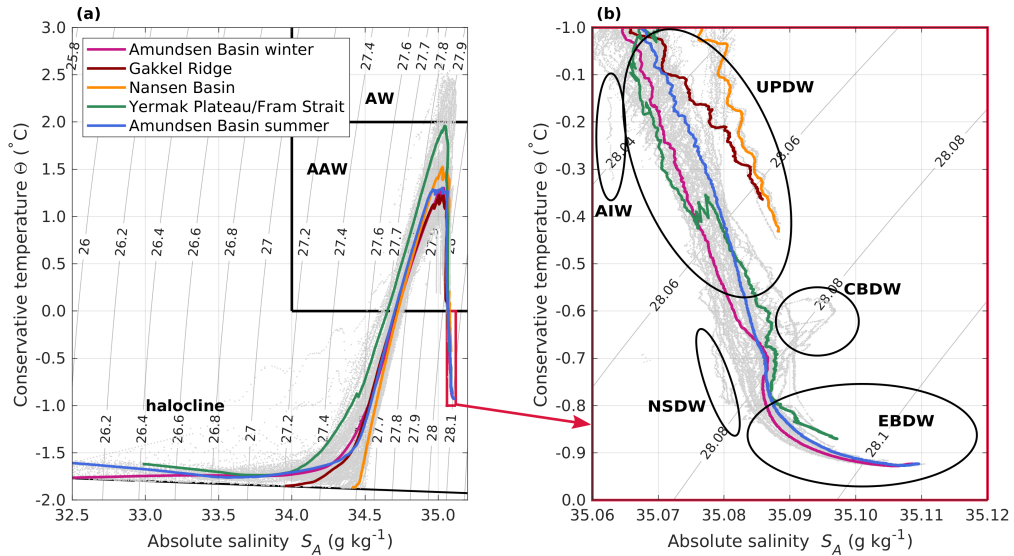


**Figure 3. Temperature-Salinity diagrams.**

Absolute salinity against conservative temperature for (a) the full depth range (for the basin averages, the upper 5 m are not shown); and (b) enlargement of the deep water masses. Gray lines indicate daily profiles and colored lines refer to basin averages as indicated. The black line in (a) indicates the salinity-dependent freezing point temperature and black rectangles indicate Atlantic Water (AW) and Arctic Atlantic Water (AAW). The small pink rectangle in (a) corresponds to the range displayed in (b). In (b), circles indicate the approximate range of Upper Polar Deep Water (UPDW), Eurasian Basin Deep Water (EBDW), Canadian Basin Deep Water (CBDW), Arctic Intermediate Water (AIW) and Nordic Sea Deep Water (NSDW).

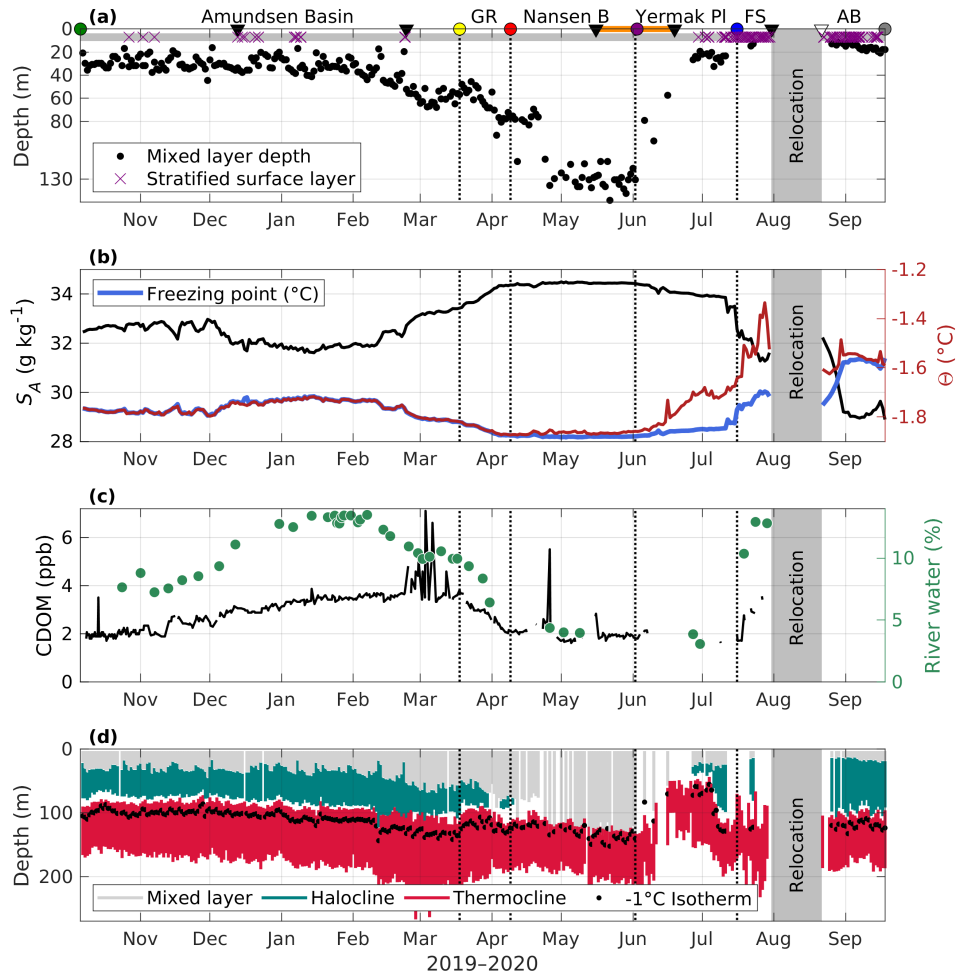


**Figure 4. Ocean surface layer properties along the drift.**

(a) Surface mixed layer depth (m, black dots, stratified surface layers are indicated with purple crosses), (b) surface absolute salinity ( $\text{g kg}^{-1}$ , black line), conservative temperature  $\Theta$  ( $^{\circ}\text{C}$ , red line) and freezing point temperature ( $^{\circ}\text{C}$ , blue line), (c) colored dissolved organic matter (CDOM, ppb, black line) and river water fraction (% , green dots) and (d) mixed layer (gray), halocline (teal) and thermocline (red) extent and position of the  $-1^{\circ}\text{C}$  isotherm (black dots) along the drift. In (a), triangles indicate the start and end of the legs, dots, vertical dotted lines and annotations the geographical markers including Amundsen Basin (AB), Gakkel Ridge (GR), Nansen Basin (B), Yermak Plateau (PI) and Fram Strait (FS). The orange line indicates the uncrewed period of the drift as in Figure 1b.

388 reflecting variable contributions from the Yenisei, Ob and Lena rivers (G Lauk-  
389 ert, unpublished). Sea ice meltwater from the preceding melt season may also  
390 contribute to a fresher surface layer in this region (compared to the water be-  
391 low) and dilute the river-borne compounds. This could explain the rather low dis-  
392 solved organic carbon (DOC) concentrations at the very start of the drift (Kong,  
393 2022). At the beginning of December, a decrease in salinity and an increase in  
394 both CDOM and river water fraction (derived from  $\delta^{18}\text{O}$ , see Section 2, sup-  
395 plemental material Text S1) to over 13 % indicate that the floe enters the river  
396 water-rich part of the Transpolar Drift. Somewhat surprisingly, the position of  
397 the maximum river water fraction does not coincide with the highest concentra-  
398 tions of CDOM, which appear only when surface salinity increases again and the  
399 surface layer starts to deepen in March (Figure 4a,b,c). This could be related to  
400 different freshwater sources and their respective advective pathways, as the dis-  
401 tribution of neodymium isotopes indicates alternating freshwater domains in this  
402 region either reflecting increased contributions from the Yenisei and Ob rivers or  
403 the Lena River (G Laukert, unpublished). A similar but spatially shifted distri-  
404 bution has already been described based on summer data from 2015, suggesting  
405 a strong spatio-temporal variability of the surface waters in the Eurasian Arctic  
406 Ocean (Paffrath et al., 2021).

407 When approaching Gakkel Ridge, the floe leaves the heavily river-water-  
408 influenced part of the Transpolar Drift and surface salinity increases to a max-  
409 imum of  $34.3 \text{ g kg}^{-1}$ . River water fraction and CDOM concentrations decrease  
410 during the passage of the ridge (Figure 4c). This is also coincident with a decrease  
411 of DOC concentrations in the surface layer (Kong, 2022). On the Nansen Basin  
412 side of the Gakkel Ridge, the surface mixed layer deepens to around 80 m. At the  
413 end of April, the surface stratification, i.e. the halocline, disappears completely  
414 and density only increases at a depth of approximately 130 m. These conditions  
415 have previously been described as "deep ventilation" (Polyakov et al., 2017), re-  
416 ferring to a mixed layer that is not bounded by the halocline but reaches down  
417 to the warm Atlantic Water layer. This enhanced connectivity between the sur-  
418 face and Atlantic layer, compared to the situation in the Amundsen Basin, is also  
419 evident from provenance tracer distributions suggesting enhanced Atlantic Water  
420 admixture to the surface (G Laukert, unpublished) and might promote the trans-  
421 port of deep oceanic heat towards the sea ice (see Section 6), thereby slowing  
422 basal growth (Lei et al., 2022) and increase vertical nutrient supply to the surface  
423 layer (Randelhoff et al., 2020). The enhanced vertical exchange might also facil-  
424 itate the transport of organisms advected in the Atlantic Water layer closer to the  
425 surface. Deep ventilation, along with relatively constant surface salinity, low river



426 water fraction and CDOM concentrations, persists throughout the Nansen Basin  
427 until the drift reaches the Yermak Plateau in June (Figure 4).

428 Above Yermak Plateau, from the end of May onwards, surface layer temper-  
429 atures increase successively with ongoing solar warming and deviate more and  
430 more from the freezing point (Figure 4b). River water fraction and CDOM remain  
431 at the same low levels as encountered in the Nansen Basin, but a slightly lower  
432 surface salinity allows for the presence of a halocline. The Atlantic Water layer  
433 on the eastern side and above the plateau is much shallower (see Section 4.3), re-  
434 stricting the vertical extent of the halocline (Figure 4d). Sea ice melt, starting in  
435 late May to early June (Webster et al., 2022; Lei et al., 2022), and surface warming  
436 create vertical density differences, i.e., stratification, within the near-surface layer.  
437 Turbulent mixing in the upper ocean (see Section 6 for details) does not penetrate  
438 deeper than 30 m and is usually not strong enough to destroy the near-surface  
439 stratification established by meltwater input and warming. Hence, especially later  
440 in the season, we often observe no classical surface mixed layer (purple crosses  
441 in Figure 4a) and even in the uppermost layer, vertical gradients in any tracer  
442 concentration, e.g., nutrients, or organism distribution, can be expected.

443 When leaving Yermak Plateau, on July 16, we observe another regime shift  
444 in the surface layer: Surface salinity abruptly decreases, while river water frac-  
445 tion and CDOM concentrations, which had remained low since entering the  
446 Nansen Basin, increase. This change is accompanied by a trend toward less ra-  
447 diogenic neodymium isotopic compositions (G Laukert, unpublished), suggesting  
448 increased admixture of Lena River water and supporting cross-Arctic transport  
449 of Siberian freshwater. In Fram Strait, we also observe a subsurface increase of  
450 CDOM (data not shown), indicative of the "edge" of the East Greenland Current  
451 (which is an extension of the Transpolar Drift of relatively fresh water of Siberian  
452 origin). Such a transition from one oceanic (surface) regime to another is often  
453 accompanied by sudden changes in biogeochemical water properties (e.g., nutri-  
454 ent relationships) and potentially also the ecological community structure (e.g.,  
455 Tippenhauer et al., 2021). Surface temperature anomaly relative to freezing point  
456 further increases, to maximum  $0.4^{\circ}\text{C}$  shortly before the floe broke up.

457 After relocation north at the end of August, back into the Amundsen Basin,  
458 we observe the freshest surface waters (see also Rabe et al., 2022) and a sta-  
459 ble halocline similar to the first phase of the drift. There are no sensor-based  
460 CDOM measurements after the relocation, but the highest CDOM absorption and  
461 DOC concentrations in surface waters during MOSAiC were found here (Kong,  
462 2022). Moreover, the highest river water fractions based on oxygen isotopes and  
463 the least radiogenic neodymium isotope signatures were determined, in line with

464 the strongest Lena River contributions during the entire MOSAiC campaign (G  
465 Laukert, unpublished). The similarity of neodymium isotope signatures between  
466 this freshwater domain and that in the western Fram Strait may suggest contin-  
467 uous freshwater transport along the Transpolar Drift. However, enhanced fresh-  
468 water export from the Siberian shelf exhibits a strong seasonality linked to the  
469 variable shelf hydrography (Janout et al., 2020), which may be preserved along  
470 the Transpolar Drift. The uppermost layer is often stratified due to sea ice melt  
471 and solar warming. Whenever a well-defined surface layer exists, it is about 20 m  
472 deep, slightly shallower than during the first part of the drift. Surface temperatures  
473 were still above freezing when sampling resumed, but approached freezing point  
474 at the beginning of September.

475 In addition, when resuming sampling after the flow was left uncrewed in July,  
476 we observed an approximately 1 m thick, low-salinity ( $S_A$  from close to 0 to  
477 about  $10 \text{ g kg}^{-1}$ ) under-ice meltwater layer, visible in salinity profiles (Schulz  
478 et al., 2022b). At the interface between the fresher meltwater layer and the under-  
479 lying colder sea water, thin layers of ice formed, so-called false bottoms (Smith  
480 et al., 2022; Salganik et al., 2023a). Low salinity meltwater layers in leads re-  
481 mains present until strong winds caused enhanced mixing between September 5–9  
482 (Smith et al., 2023; Nomura et al., 2023). The presence of meltwater results in a  
483 very strong stratification in the uppermost meters, up to two orders of magnitude  
484 stronger compared to the halocline. Measurements with an uprising turbulence  
485 profiler also show drastically reduced turbulent mixing in the near-surface layer  
486 when meltwater layers were present Fer et al. (2022). Details on the dynamics  
487 and implications of meltwater layers can be found in Smith et al. (2023, 2022);  
488 Salganik et al. (2023a); Nomura et al. (2023).

### 489 4.3. *Atlantic Water layer along the MOSAiC drift*

490 Modified Arctic Atlantic Water (AAW) is present throughout the MOSAiC drift.  
491 In the Amundsen Basin, the upper limit of the AAW layer is situated at approxi-  
492 mately 150 m depth. After passing the Gakkel Ridge into the Nansen Basin, the  
493 AAW is warmer and situated deeper in the water column (Figure 2a). Relatively  
494 unmodified Atlantic Water (AW), coming straight from the Atlantic and being  
495 characterized by a core temperature above  $2^\circ\text{C}$ , is only present above Yermak  
496 Plateau (Figure 2c), where warm waters also reside about 100 m closer to the sur-  
497 face (Figure 4d), and in Fram Strait. In this manuscript, we use the term Atlantic  
498 Water (layer) to refer to both AW and AAW.

499 The "older" the Atlantic Water layer, i.e., the longer it has not been in contact

500 with the surface and traveled in the Arctic while being mixed with colder wa-  
501 ters, the deeper and colder its core (Rudels, 2015). Hence, we observe a strong  
502 correlation ( $R^2 = 0.67$ , not shown) between the core depth and the core temper-  
503 ature. Along the drift in 2019–2020, the Atlantic Water core was mostly located  
504 at around 300 m depth, with a temperature around 1.2°C. Above Yermak Plateau  
505 and in Fram Strait, the core is approximately 1°C warmer (and 0.1 kg m<sup>-3</sup> lighter)  
506 and 100 m shallower, but subject to strong variability. In this region, the impact  
507 of the shallow and "young" Atlantic Water on e.g., nutrient supply or organism  
508 composition, might be more pronounced compared to the situation in the deep  
509 basins.

510 As Atlantic Water can take different paths within the Arctic Ocean, e.g., en-  
511 tering via Fram Strait or through the Barents Sea, or recirculating into the deep  
512 basins from different positions along the continental slope (Rudels et al., 2012;  
513 Rudels, 2015), different branches of Atlantic Water, with slightly different tem-  
514 perature and salinity signatures, can often be found at the same position, stacked  
515 on top of each other (Rudels and Hainbucher, 2020). These "interleaving" layers  
516 can be identified as z-shapes near the Atlantic Water temperature maximum in  
517 the TS-diagrams (Figure 3a) and as inversion layers and local temperature min-  
518 ima in the temperature profiles. In the Amundsen and Nansen Basin, interleaving  
519 involves mainly the Barents Sea and the Fram Strait branches of Atlantic Water.  
520 In the more dynamic Fram Strait region, we find strong interleaving, with several  
521 sources of Atlantic Water, which might differ in their respective biogeochemical  
522 signature that cause vertical gradients in, e.g., nutrient concentration.

523 In addition, at the upper bound of the Atlantic Water layer, both temperature  
524 and salinity increase with depth. In quiescent conditions, i.e., when turbulent mix-  
525 ing is negligible and molecular diffusion is the dominant mixing process, temper-  
526 ature gradients diffuse faster than gradients in salinity. This difference in thermal  
527 and haline diffusion coefficients creates step-like structures, so-called thermoha-  
528 line or double-diffusive staircases, typical for the Arctic Ocean (Shibley et al.,  
529 2017). These structures can persist for years and over 100 km of horizontal dis-  
530 tance and individual layers can be up to several 10 m thick (e.g., Lenn et al.,  
531 2009; Guthrie et al., 2017). Along the MOSAiC drift, we frequently, but not al-  
532 ways, observe thermohaline staircases in the quiescent Amundsen Basin, in line  
533 with findings from high resolution observations from drifting stations in the same  
534 area, that show 1–3 m thick thermohaline staircase layers in the 200–260 m depth  
535 range (Sirevaag and Fer, 2012). Outside of the Amundsen Basin, we sometimes  
536 see structures that might be remnants of thermohaline staircases in the vertical  
537 profiles (not shown), but their characteristic sharp interfaces are absent. These

538 differences point towards a lower connectivity between the surface and deeper  
539 ocean in the Amundsen Basin, compared to the other parts of the drift.

#### 540 *4.4. Deep water along the MOSAiC drift*

541 The deep water masses during the MOSAiC drift are already described in detail in  
542 Karam et al. (2023) and Rabe et al. (2022) and we only provide a brief summary  
543 here. Despite the uncertainties associated with the identification of deep water  
544 masses (sensor accuracy, changes in end member properties, see Section 4.1), we  
545 observe a somewhat consistent distribution of deep waters across the Eurasian  
546 basin during MOSAiC. In the Nansen and Amundsen Basin, we see UPDW right  
547 under the Atlantic layer down to approximately 1500 m. Below the UPDW, we pri-  
548 marily find EBDW until the sill depth of Fram Strait (approximately 2500 m) and  
549 we occasionally see intrusions of relatively warm and saline CBDW as a salinity  
550 maximum between 1700–2000 m depth (Karam et al., 2023). Below the sill depth  
551 of Fram Strait, the temperature increases slightly as we encounter the last deep  
552 water mass, EBBW, until the sea floor. Deep waters directly above Gakkel Ridge  
553 and their unique hydrothermal-vent-influenced ecosystem were not sampled dur-  
554 ing MOSAiC.

555 The deeper waters above Yermak Plateau and in Fram Strait consist of UPDW,  
556 alternating with likely AIW. Below UPDW/AIW, we can again observe CBDW  
557 in Fram Strait, as a salinity maximum at roughly 2000 m depth. Close to the  
558 bottom in Fram Strait, we find a mixture of NSDW and EBDW. Again, we note  
559 that identifying water masses in Fram Strait solely based on their temperature  
560 and salinity signature as done in this study is associated with large uncertainties,  
561 primarily due to the warming and increased salinity of waters south of Fram Strait  
562 over the past decades. Hence, traditional water mass classifications (Marnela et al.,  
563 2016) do not necessarily hold for the deep waters anymore (Somavilla et al., 2013;  
564 von Appen et al., 2015). Other tracers, such as CFC, SF<sub>6</sub>, or dissolved oxygen, are  
565 needed to accurately determine the origin of deep water masses, which is beyond  
566 our scope and addressed in Karam et al. (2023) and Heuzé et al. (2023a).

### 567 **5. Current velocities, tides and eddies**

568 In both central basins, current velocities below the surface mixed layer are small,  
569 on the order of 0.01 m s<sup>-1</sup>. Within the surface mixed layer, current velocities are  
570 intensified and correlate with the sea ice drift speed ( $R^2=0.9$ , data not shown). The  
571 magnitude of the ocean surface current (14–30 m vertical average), however, is  
572 much smaller, on average 16 % of the floe drift speed (Figure 5a), meaning the ice

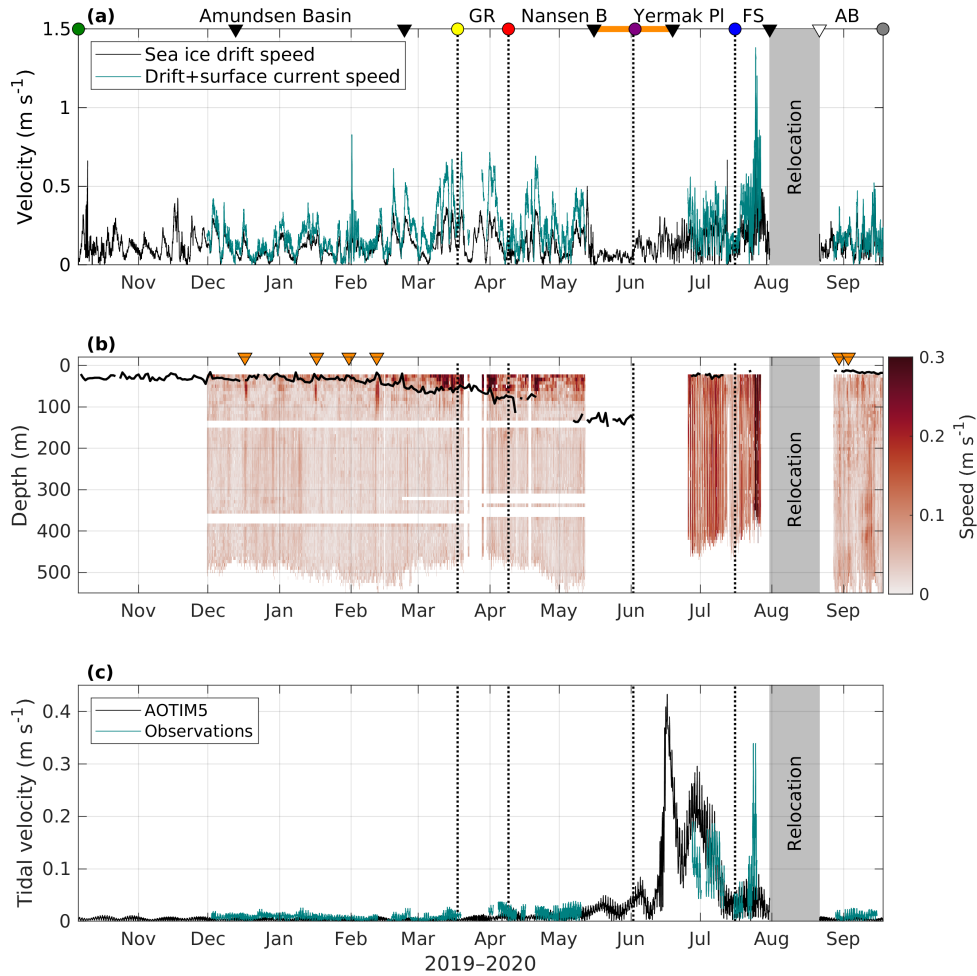


**Figure 5. Current velocities along the drift.**

(a) Sea ice drift (black,  $\text{m s}^{-1}$ ) and combined drift and averaged current velocity in the upper 14–30 m relative to the floe (teal,  $\text{m s}^{-1}$ ), (b) current speed ( $\text{m s}^{-1}$ ) relative to the sea floor and (c) tidal velocities ( $\text{m s}^{-1}$ ) from observations (teal) and the Arctic Ocean Tidal Inverse Model AOTIM5 (black) along the drift. In (a), triangles indicate the start and end of the legs, dots, vertical dotted lines and annotations the geographical markers including Amundsen Basin (AB), Gakkel Ridge (GR), Nansen Basin (B), Yermak Plateau (PI) and Fram Strait (FS). The orange line indicates the uncrewed period of the drift as in Figure 1b. In (b), orange triangles indicate near-surface eddies, the black line indicates the depth of the surface mixed layer.

573 moves around six times faster than the upper ocean. This difference illustrates that,  
 574 while both sea ice and fresh, riverine water are transported from their region of  
 575 origin in Siberia across the Arctic towards Fram Strait, their transport timescales  
 576 and exact pathways differ. Sea ice within the Transpolar Drift typically traverses  
 577 the Arctic Ocean within 1–3 years (Charette et al., 2020; Steele et al., 2004), while  
 578 the transport timescale for fresh water might be rather on the order of a decade.  
 579 In addition, the pathway of the Transpolar Drift is strongly influenced by daily  
 580 to decadal variability in wind conditions (Mysak, 2001), yielding that liquid and  
 581 solid freshwater of similar origin in space and time might take very different routes  
 582 through the Arctic Ocean. The difference in sea ice drift and surface ocean current  
 583 speed also underlines that, while sampling the same sea ice, the water below the  
 584 ice quickly changes throughout the drift and oceanic data cannot be treated as a  
 585 simple time series. Furthermore, as the surface mixed layer tends to move faster  
 586 than the ocean below, any time series recorded above and below the surface mixed  
 587 layer base might develop independently of each other.

588 The region around Yermak Plateau and especially in Fram Strait, is more en-  
 589 ergetic. Absolute current velocities are much higher (up to  $0.4 \text{ m s}^{-1}$ ) and more  
 590 variable and surface currents correlate less with sea ice drift. Here, tides play a  
 591 greater role, with a dominance of diurnal frequencies above Yermak Plateau and  
 592 semi-diurnal frequencies in Fram Strait (data not shown, see Fer et al., 2015, for  
 593 details on tides in the region). In combination with the more variable water col-  
 594 umn structure in this region (see Section 4), we expect more variability on short,  
 595 daily to sub-daily, timescales, e.g., in surface nutrient supply or species composi-  
 596 tion. Assumptions of lateral homogeneity, i.e., negligible spatial gradients, which  
 597 are to some degree justified in the respective deep basins, do not hold anymore in  
 598 the dynamic regime of Yermak Plateau and Fram Strait.

**Table 2. Clearly identifiable upper ocean eddies along the drift.**

Start	End	$D^a$ (m)	$\Delta h^b$ (m)	Type
17.12.19 01:00	18.12.19 11:00	38	40	Anticyclonic
16.01.20 07:00	17.01.20 10:00	38	48	Anticyclonic
31.01.20 08:00	02.02.20 07:00	22	56	Anticyclonic
11.02.20 14:00	13.02.20 12:00	22	80	Anticyclonic
29.08.20 17:00	30.08.20 17:00	38	40	Cyclonic
03.09.20 23:00	03.09.20 10:00	30	64	Anticyclonic

<sup>a</sup> First depth where the eddy is detected.

<sup>b</sup> Vertical eddy thickness.

599 Six upper ocean eddies were identified in the halocline in the Amundsen and  
600 Nansen Basin, listed in Table 2 and indicated in Figure 5b. Five of these eddies  
601 rotated anticyclonically (clockwise) and only one cyclonically, in line with the  
602 previously reported prevalence of anticyclonic eddies in the Arctic Ocean (Zhao  
603 et al., 2014; von Appen et al., 2022). The timing of these eddies does not coincide  
604 with the presence of storms or strong winds, indicating the eddies have not been  
605 formed locally, but might rather be advected and originate from topographic fea-  
606 tures (Zhao et al., 2014) or barotropic and baroclinic instabilities (von Appen et al.,  
607 2022). Eddies can transport water masses with distinct biogeochemical signatures  
608 over large distances and their associated higher current velocities can increase lo-  
609 cal vertical mixing (Son et al., 2022). Both processes can enhance the nutrient  
610 supply to the photic zone, making eddies potential biological hotspots. Any nu-  
611 trients supplied by eddy activity in the Arctic winter would not be consumed, but  
612 (locally) increase the nutrient inventory for the next productive season. In addi-  
613 tion, anticyclonic eddies are associated with a shoaling of the mixed layer base,  
614 most pronounced for the eddies in January and February, where the mixed layer  
615 depth decreased by 10–20 m. However, a similar variability in mixed layer depth  
616 is also observed during times when eddies were absent. In the Yermak Plateau/  
617 Fram Strait regions, eddy activity is obscured by the strong tides; hence no eddies  
618 were identified there.

619 On November 9, 14 and 28 (2019), we also observed a large anticyclonic eddy  
620 at greater depth in the middle of the Amundsen Basin, indicated by sloping isopy-  
621 cnals above and below the eddy, with relatively dense waters above the eddy and  
622 light waters below, relative to the adjacent water column (data not shown). The  
623 eddy carries a warm and saline CBDW intrusion and extends over approximately  
624 1200–2400 m depth (Karam et al., 2023).

## 625 6. Turbulence and vertical transport

### 626 6.1. *Surface mixing*

627 In contrast to the surface *mixed* layer depth, which describes the depth to which  
628 the surface layer is uniform in temperature and salinity (see Section 4.2), the *mix-*  
629 *ing* layer depth describes how deep active turbulent mixing, which is created by  
630 friction at the ice-ocean interface, or by wind and waves in the marginal ice zone  
631 or open water conditions, penetrates into the water column. While active mixing  
632 creates the mixed layer by homogenizing the water column, the mixed layer will  
633 persist even after the active mixing has decayed. That is because the small-scale  
634 turbulent motion causing the mixing will dissipate within hours or days, but the

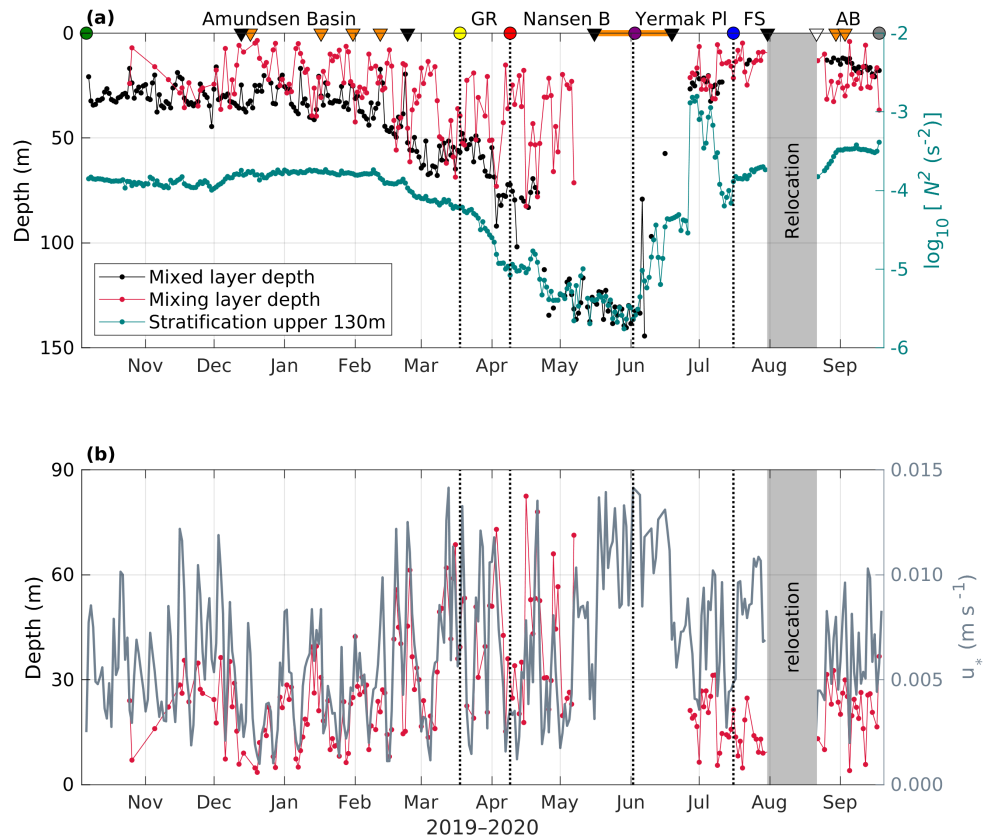


**Figure 6. Parameters related to surface turbulence along the drift.**

(a) Surface mixed layer depth (black) and mixing layer depth (red, m, left vertical axis) and upper ocean stratification (teal, right axis,  $\text{s}^{-2}$ ). (b) Mixing layer depth (red, m, left axis; note that the vertical axis is reversed) and friction velocity (gray, right axis). In (a), black and white triangles indicate the start and end of the legs, dots, vertical dotted lines and annotations the geographical markers including Amundsen Basin (AB), Gakkel Ridge (GR), Nansen Basin (B), Yermak Plateau (PI) and Fram Strait (FS). The orange line indicates the uncrewed period of the drift as in Figure 1b and orange triangles indicate near surface eddies.



635 re-establishment of gradients near the surface, i.e. re-stratification, often takes  
636 much longer, especially in the absence of restoring forces, such as strong lateral  
637 gradients. This is the reason why the distribution of biological and biogeochemi-  
638 cal tracers is often homogeneous in the actively mixing layer, but not in the mixed  
639 layer, where it instead reflects a combined signal of past active mixing and new  
640 biological production (or consumption) in the respective layers (Carranza et al.,  
641 2018).

642 This relation between the depth of the mixed and active mixing layer is illus-  
643 trated in Figure 6a. At times, active mixing reaches down to the base of the mixed  
644 layer, but is often confined to the upper 20 m. In the Nansen Basin, in the presence  
645 of deep ventilation conditions, active mixing occasionally reaches down to a max-  
646 imum of 80 m, but not to the mixed layer base located at approximately 130 m.  
647 However, we have limited observations of turbulence here, due to the interruption  
648 of the drift between legs 3 and 4. Upon return to the Amundsen Basin in summer,  
649 the mixed layer depth is shallower compared to the winter condition, caused by a  
650 lower surface salinity and hence stronger upper ocean stratification (teal line, Fig-  
651 ure 6a). The active mixing layer depth, however, is comparable to the maximum  
652 depth of active mixing typically observed in this region in winter, during the first  
653 part of the drift, and reaches *deeper* than the mixed layer base. In other words,  
654 the same level of turbulent energy that created an approximately 30 m deep mixed  
655 layer in the presence of weaker upper ocean stratification (first part of the drift),  
656 only created a 20 m deep mixed layer in the presence of stronger stratification (last  
657 part of the drift). This illustrates how strong stratification requires more turbulent  
658 energy to be mixed and that storm events, associated with elevated levels of turbu-  
659 lence, can have a different impact on the vertical transport of, e.g., nutrients and  
660 other biogeochemical compounds or organisms, depending on the strength of the  
661 upper ocean stratification.

662 As the turbulent energy in the mixing layer mainly originates from friction at  
663 the ice-ocean interface, the depth of the mixing layer is, to a large extent, related to  
664 the sea ice drift speed. A parameter to describe the impact of drift speed on upper  
665 ocean turbulence is the friction velocity,  $u_*$  (Figure 6b, right vertical axis). In the  
666 (winter) Amundsen Basin and in the Nansen Basin, the evolution of the mixing  
667 layer depth corresponds to variations in friction velocity, on a daily time scale.  
668 The relationship is different, but still visible, above Yermak Plateau and breaks  
669 down in the Fram Strait. Both regions are characterized by considerably higher  
670 current velocities, which likely contribute to the friction at the ice-ocean interface.  
671 Furthermore, sea ice melt has probably reduced the bottom roughness of the sea  
672 ice (which has been kept constant in the  $u_*$  calculation here), thereby reducing the

673 efficiency of energy transfer from sea ice drift to surface ocean turbulence. After  
674 resuming sampling on another ice floe in the Amundsen Basin in late summer,  
675 in the presence of a stronger upper ocean stratification, the mixing layer depth is  
676 relatively constant and the effect of the friction velocity is less clear. In summary,  
677 variations in ice drift speed strongly influence the mixing layer depth on daily or  
678 probably shorter time scales, but other effects like the upper ocean stratification  
679 and tides are likely to alter this relationship.

680 The different timescales on which the active mixing and the mixed layer depth  
681 vary can have implications for the distribution of tracers and organisms in the  
682 near-surface layer. During longer calm periods, when the wind and drift speed  
683 are low, vertical biogeochemical gradients might be established within the sur-  
684 face mixed layer, e.g., if nutrients are preferentially consumed in the upper part  
685 of the mixed layer, where more sunlight is available, or if tracers and organisms  
686 from melting sea ice are injected to the ocean and accumulate only in the very  
687 top layer. A wind event can then easily homogenize these gradients on very short  
688 (hourly) timescales, altering the biogeochemical signature over the whole mixed  
689 layer depth. Such an event could boost primary productivity, by replenishing sur-  
690 face nutrients, but could also have an adverse effect by displacing organisms to  
691 greater depths, where less sunlight is available and food is more diluted.

## 692 6.2. *Turbulent diffusivity*

693 The decay of turbulent energy with increasing distance from the surface, where  
694 it is generated mainly by friction under the sea ice, is visible in Figure 7a. In  
695 the Amundsen Basin, strong stratification (Figure 7b) confines elevated levels of  
696 mixing to the upper approximately 70 m in winter and, due to stronger surface  
697 stratification, to approximately 50 m in summer. In the Nansen Basin, where the  
698 upper ocean is well mixed or only weakly stratified (yellow lines in Figure 7),  
699 turbulence is elevated in the upper 90 m and still slightly above noise level down  
700 to approximately 200 m. The Yermak Plateau and Fram Strait regions are more  
701 stratified, partly due to buoyancy input by meltwater and solar warming, but also  
702 more dynamic (see Section 5). Here, turbulence is strongly elevated in the upper  
703 40 m and still elevated, but weaker than in the Nansen Basin, below.

704 Vertical diffusivity, the coefficient necessary to calculate turbulent vertical  
705 fluxes in the presence of stratification, differs both regionally and depending on  
706 the vertical position in the water column. In the strongly stratified halocline in the  
707 Amundsen Basin, values are smallest and on the order of  $10^{-6} \text{ m}^2 \text{ s}^{-1}$ , as already  
708 reported in Schulz et al. (2023a), illustrating how the halocline separates the sur-

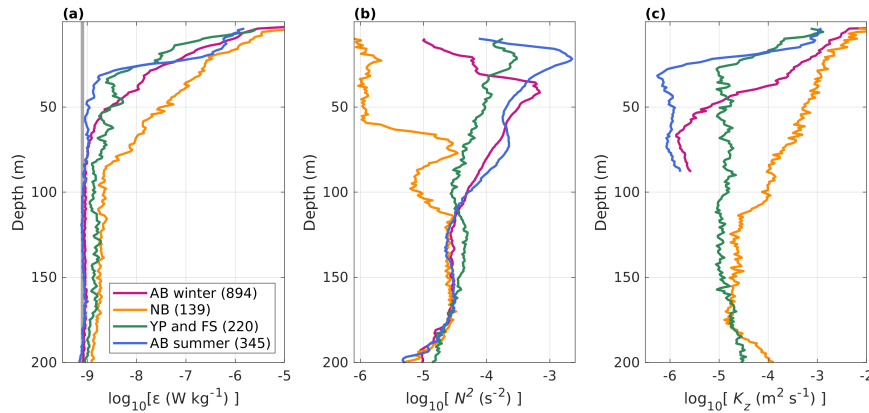


**Figure 7. Turbulence and stratification profiles.**

Basin-averaged vertical profiles of the (a) turbulent dissipation rate  $\varepsilon$  ( $\text{W kg}^{-1}$ ), (b) Brunt-Väisälä frequency,  $N$ , squared ( $\text{s}^{-2}$ ) and (c) vertical diffusivity  $K_z$  ( $\text{m}^2 \text{s}^{-1}$ ). Colors refer to the Amundsen Basin (AB) summer and winter conditions, Nansen Basin (NB) and the Yermak Plateau (YP) and Fram Strait (FS) averages, the vertical gray line in (a) indicates the lowest detection (“noise”) level of the profiler. Data below around 90 m in the Amundsen Basin and below 200 m in the Nansen Basin and the Yermak Plateau and Fram Strait regions are at noise level and not shown in (c).

709 face from the deeper water layers. In the conditions we encountered in summer,  
 710 characterized by lower surface salinity and a shallower mixed layer, the “bottle-  
 711 neck” for vertical transport formed by the halocline is even more pronounced (blue  
 712 and violet lines in Figure 7c). In the Yermak Plateau and Fram Strait regions, up-  
 713 per ocean (30–160 m) vertical diffusivity is an order of magnitude higher, around  
 714  $10^{-5} \text{ m}^2 \text{ s}^{-1}$  (green line in Figure 7c). In the Nansen Basin, upper ocean vertical  
 715 diffusivity is highest, ranging from more than  $10^{-3} \text{ m}^2 \text{ s}^{-1}$  in the upper 50 m, grad-  
 716 ually decreasing to approximately  $10^{-5} \text{ m}^2 \text{ s}^{-1}$  at around 170 m depth. Highest  
 717 vertical fluxes of any tracer, e.g., heat, nutrients or oxygen, are therefore expected  
 718 in the Nansen Basin.

719 The variability within both basins is relatively low and average values are a  
 720 good representation of the typical conditions. However, the Yermak Plateau and  
 721 Fram Strait regions are energetic and exhibit considerably different conditions,  
 722 e.g., with respect to tidal currents (Section 5), stratification and Atlantic Water  
 723 layer properties (Section 4). Here, average values can be informative and descrip-

724 tive, but for detailed studies in those regions, the actual contemporaneous condi-  
725 tions need to be considered.

### 726 6.3. *Heat fluxes*

727 Ocean heat fluxes presented here were calculated in two ways. Close to the sur-  
728 face (3 m depth), high-resolution point measurements of three-dimensional veloc-  
729 ity and temperature from an autonomous buoy provide heat fluxes based on direct  
730 eddy correlation methods. In deeper layers, we can derive heat fluxes from vertical  
731 temperature gradients and the vertical diffusion coefficient  $K_z$  (described above),  
732 e.g., over the halocline or the Atlantic Water thermocline (see Section 2, supple-  
733 mental material Text S1). The heat flux at 3 m reflects how small difference in  
734 heat, i.e., water even slightly above the local salinity-controlled freezing point, is  
735 transported near the ice-ocean interface. The heat flux over the halocline describes  
736 the heat entering the surface mixed layer from the ocean below. The heat flux over  
737 the thermocline can be interpreted as the heat lost from the Atlantic Water to the  
738 colder water layer above (Schulz et al., 2021). Similarly, vertical fluxes of other  
739 tracers, e.g., nutrients or dissolved oxygen, could be calculated from the  $K_z$  data  
740 presented here and the respective tracer profiles. Depending on the position of  
741 the layer of interest, e.g., the nitracline, we expect that these fluxes qualitatively  
742 follow the variability we observe in heat fluxes.

743 Heat fluxes at 3 m depth, near the top of the ocean mixed layer (Figure 8a),  
744 range between  $-2$  and  $7 \text{ W m}^{-2}$  and exhibit a typical wide day-to-day variabil-  
745 ity, arising primarily from the variable wind-forced motion of the ice (Figure 5a).  
746 During the winter period, in the absence of solar heating, the 3 m fluxes arise  
747 from wind-ice-forced turbulent mixing of heat within the mixed layer and heat  
748 trapped by the strong salinity-controlled density gradient at the base of the mixed  
749 layer. Heat transport from the base of the mixed layer is strongly amplified in the  
750 presence of eddies. During the ice growth period (December to end of April), ice  
751 basal growth of 0.92 m to 1.05 m was measured (AOFB altimeter on a different  
752 floe, Perovich et al. (accepted)). This basal growth is dominated by ice conductive  
753 fluxes controlled by air temperature, humidity, wind speed, the effects of highly  
754 insulating snow, ice thickness and ice salinity. Since the ocean mixed layer tem-  
755 perature is very close to the freezing point (Figure 4b in Section 4.2), heat lost  
756 to the ice cannot further cool the ocean, but rather forms ice, releasing brine and  
757 removing latent heat from the ice-water interface (e.g., McPhee, 2008). The small  
758 contribution to ice basal change from time-integrated predominantly upward heat  
759 fluxes for this timeseries was just 1.2 cm of ice loss, with little contribution after

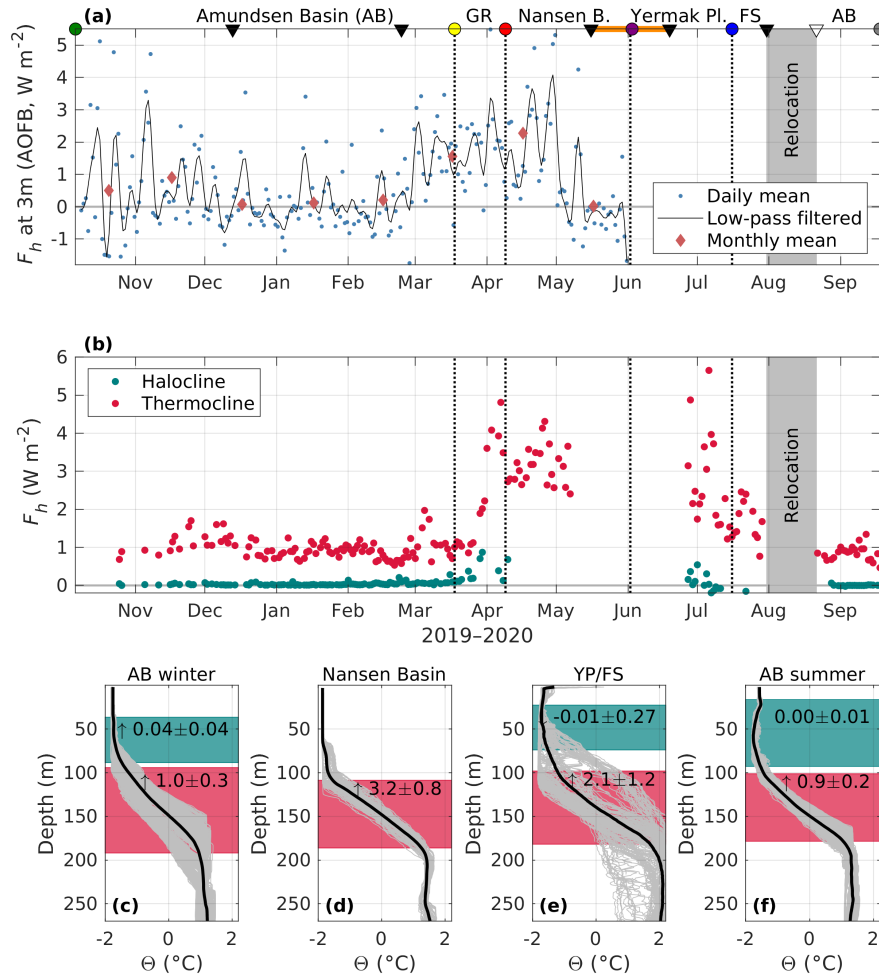


**Figure 8. Vertical heat fluxes during the drift.**

(a) Heat fluxes ( $F_h$ ) at 3 m depth, based on eddy-correlation, measured with an Autonomous Ocean Flux Buoy (AOFB) at the Distributed Network "L2" site (Rabe et al., 2022), in a distance of 15–25 km from *Polarstern*. Blue dots are daily averages, the black line is a 6-day low-pass filtered timeseries and red diamonds are monthly mean flux values. (b) Heat fluxes over the halocline (teal dots) and Atlantic Water thermocline (red dots) based on shear probe measurements. (c)-(f) Individual (gray) and average (black) conservative temperature ( $\Theta$ ) profiles and average halocline and thermocline heat fluxes in the Amundsen Basin (AB) in summer and winter, the Nansen Basin and the Yermak Plateau and Fram Strait regions (YP/FS). All values are in  $W m^{-2}$ . In (a), triangles indicate the start and end of the legs, dots, vertical dotted lines and annotations the geographical markers including Gakkel Ridge (GR), Nansen Basin (B), Yermak Plateau (PI) and Fram Strait (FS). The orange line indicates the uncrewed period of the drift as in Figure 1b.

760 the beginning of May 2020.

761 As previously reported, based on the winter Amundsen Basin data from MO-  
762 SAiC (Schulz et al., 2023a), the heat flux over the halocline is negligible, meaning  
763 that the halocline effectively shelters the upper water layers and the sea ice from  
764 the heat in the Atlantic Water layer. While there is a minimal upward flux in the  
765 Amundsen Basin in winter, though with heat fluxes much smaller than  $0.1 \text{ W m}^{-2}$ ,  
766 the stronger stratification present in summer completely suppresses any heat trans-  
767 port over the halocline (Figure 8a,c,f). When approaching the Gakkel Ridge in  
768 March, halocline heat fluxes gradually increase and reach maximum levels above  
769 the ridge. However, daily mean values are still small, below  $0.8 \text{ W m}^{-2}$  (directed  
770 upwards). Halocline heat fluxes above the Yermak Plateau are comparable to those  
771 above the Gakkel Ridge, until surface heating reverses the temperature gradient  
772 and we observe small, downward-oriented heat fluxes.

773 Upward heat loss from the Atlantic Water layer in the Amundsen Basin is  
774 around  $1 \text{ W m}^{-2}$ , with little (sub)seasonal variability. Under deep ventilation con-  
775 ditions in the Nansen Basin, in the absence of a sheltering halocline, the more  
776 turbulent surface layer directly connects with the Atlantic Water layer and ther-  
777 mocline heat fluxes are increased by a factor of three, compared to the Amundsen  
778 Basin conditions with a stable halocline (Figure 8b,c,d,f). In the Yermak Plateau  
779 and Fram Strait regions, heat fluxes are also enhanced, but the temperature struc-  
780 ture in the water column, and hence the heat flux, is more variable (Figure 8c).  
781 Here, heat fluxes are highest on the plateau, where the Atlantic Water layer is  
782 shallow and the Atlantic Water core is warmer (and younger) compared to the rest  
783 of the drift. Heat fluxes decrease to a level between Nansen and Amundsen Basin  
784 conditions when entering Fram Strait.

## 785 7. Comparison of MOSAiC data and ocean climatologies

786 Ocean climatologies are interpolations of observed temperature and salinity pro-  
787 files, which are often used as initial or boundary conditions in modeling studies,  
788 or for ground-truthing the results of simulations. In contrast, state estimates are  
789 realizations of numerical models that have been optimized to best fit observa-  
790 tional data, while obeying the physical laws that govern processes in the ocean.  
791 The majority of data used to create the climatologies were collected more than 10  
792 years ago (Table 1) and since the Arctic is the world's fastest-changing region, it is  
793 unclear how representative these datasets still are. The high-resolution MOSAiC  
794 data can serve as a benchmark for the "modern-day" Eurasian Arctic, enabling  
795 us to evaluate how representative the climatologies are of the current conditions.

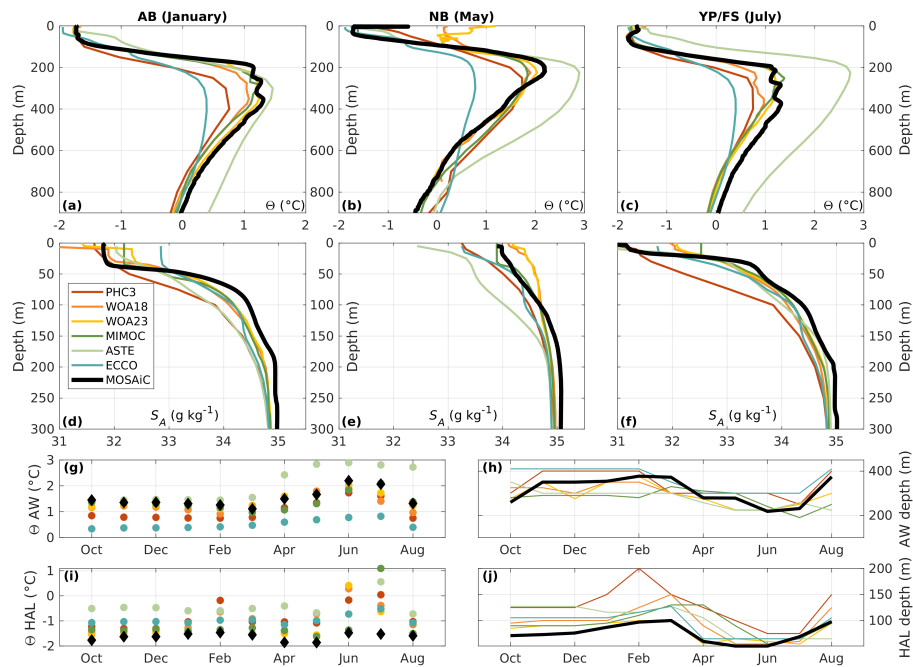


**Figure 9. Comparison of the observations along the drift with climatological datasets and state estimates.**

(a,b,c) Conservative temperature ( $\Theta$ ) and (d,e,f) absolute salinity profiles of four climatological datasets (PHC3, WOA18, WOA23 and MIMOC) and two state estimates (ECCO and ASTE, see Section 2 and supplemental material Text S1 for details) and the MOSAIC observations. Note the different ranges on the y-axis for salinity and temperature. Data have been averaged for the months of January in the Amundsen Basin (AB), May in the Nansen Basin (NB) and July in the Yermak Plateau and Fram Strait regions (YP/NB). Atlantic Water (AW) core (g) conservative temperature ( $\Theta$ ) and (h) depth (m) and halocline (HAL) (i) conservative temperature ( $\Theta$ ) and (j) depth (m).

796 Here, we compare four climatologies and two state estimates in three time periods/  
797 regions (Figure 9) to the new MOSAiC data. We calculated month-long averages  
798 of the MOSAiC data, with the January average representing Amundsen Basin  
799 winter conditions, May representing spring conditions in the Nansen Basin, and  
800 July representing summer conditions in the Fram Strait region. The correspond-  
801 ing climatological averages were derived from the objectively analyzed monthly  
802 datasets of each climatology/state estimate, utilizing the nearest climatology grid  
803 cell to the drift location at the midpoint of the corresponding month. For additional  
804 information, including details about the respective data sources for the climatolo-  
805 gies, see supplemental material Text S1.

806 Overall, we find good agreement between the climatologies and MOSAiC  
807 data, regarding the vertical structure and seasonal and regional variability. The  
808 MIMOC and WOA18 climatology show strong agreement and similarity, despite  
809 WOA18 containing a larger proportion of older data compared to MIMOC. The  
810 two state estimates, ECCO and ASTE, accurately reconstruct the complex ver-  
811 tical structure and the halocline, as well as seasonal and regional changes. Not  
812 all climatologies accurately represent the surface mixed layer, which is subject to  
813 considerable short-term variability, as profiles were often averaged over different  
814 regions and time periods. MIMOC is the only climatology that considers this issue  
815 during the interpolation and objective mapping process.

816 PHC3, with the oldest data of all the data products considered here (Ta-  
817 ble 1), features a fresher Atlantic layer and halocline, compared to other data  
818 products and MOSAiC data, which is expected as most data is pre-Atlantification  
819 (Polyakov et al., 2017). The state estimates ECCO and ASTE are subject to tem-  
820 perature biases in the Atlantic layer, with ECCO being 1–1.5°C colder and ASTE  
821 being 0.2–2.0°C warmer (with a larger bias in spring/summer Eurasian Basin than  
822 in the winter Amundsen Basin), compared to the observed Atlantic Water core.  
823 ASTE also exhibits a salinity bias, with a fresher Atlantic Water and halocline  
824 layer, resulting in a weaker stratification. These biases point to issues reproducing  
825 the Atlantic Water pathway (a common issue in many models, e.g., Heuzé et al.  
826 (2023b); Wang et al. (2023)), an underestimation of vertical heat fluxes from the  
827 Atlantic Water layer and not enough observations along the Eastern Arctic bound-  
828 ary current available to constrain the model (Nguyen et al., 2021). Constraining a  
829 new release of ASTE with MOSAiC data will likely reduce this bias.

830 Across all basins and seasons, the MOSAiC data consistently exhibit warmer  
831 Atlantic Water, compared to the climatologies. The climatologies demonstrate a  
832 clear temporal dependency, with PH3, containing the oldest data, featuring the  
833 coldest Atlantic Water, approximately 1°C colder compared to the most recent



834 WOA23. This observation aligns with the expected consequences of rapid Arctic  
835 Amplification and Arctic Ocean warming (Rantanen et al., 2022). Another pos-  
836 sible shift is indicated in the Amundsen Basin halocline properties, the extent of  
837 which decreases from 130–200 m in the (oldest) PHC3 climatology to 70–100 m  
838 during MOSAiC. This shift is in line with previous findings of a weakening and  
839 shallowing of the halocline over recent decades (Polyakov et al., 2020a).

840 However, MOSAiC data is a snapshot of only one year and does not capture  
841 interannual or decadal variability (e.g., Polyakov et al., 2023). The identification  
842 of long-term variability and/or climate-change induced changes in water mass  
843 properties at all depths is not trivial. It requires in-depth analyses of variability and  
844 changes in both the upstream (e.g., properties in and exchanges with the Nordic  
845 Seas) and the internal (e.g., shelf ventilation) processes. Such analyses can only  
846 be done by comparing MOSAiC to several decades of scarce, historical data and  
847 are beyond the scope of this study. We also note that, consistent with previous  
848 studies (e.g., Timmermans and Marshall, 2020), we observe significant regional  
849 disparities within the Arctic Ocean, surpassing temporal variations on both short  
850 and long-term timescales. Therefore, while the MOSAiC data reflect conditions in  
851 the Eurasian basins, it is not necessarily representative of modern-day conditions  
852 elsewhere in the Arctic (see also Section 9).

## 853 8. Discussion

### 854 8.1. *MOSAiC findings in comparison with previous results*

#### 855 8.1.1. Surface waters

856 Upper ocean properties along the MOSAiC drift were strongly influenced by the  
857 relative position of the sampling within or outside of the river water-rich Trans-  
858 polar Drift. A direct comparison to earlier observations is challenging, as the ex-  
859 act pathway of river water is subject to seasonal and interannual variability (e.g.,  
860 Mysak, 2001; Karcher et al., 2012) and sampling locations of previous expedi-  
861 tions or ITP drift tracks differ from the MOSAiC locations. At the beginning  
862 of the MOSAiC drift, the mixed layer salinity in the eastern Amundsen basin,  
863 around  $32 \text{ g kg}^{-1}$  (Figure 4b), appears to be higher than in the early 2010's in  
864 the same area: Observations from late summer in 2011 (Polarstern expedition  
865 PS78, Gonçalves-Araujo et al., 2018) and 2012 (ITP64, Stedmon et al., 2021)  
866 show a fresher surface layer with salinity around  $30 \text{ g kg}^{-1}$  and a higher CDOM  
867 loading, indicative of larger presence of river runoff in the easternmost Amund-  
868 sen basin. Similar conditions were observed in 2015 (Polarstern expedition PS94,  
869 Stedmon et al., 2021)). This difference in surface salinity and CDOM concentra-

870 tion might indicate that the first part of the MOSAiC drift was rather intersecting  
871 the "edge" of the river water-rich Transpolar Drift and not the core, where surface  
872 salinity would likely be closer to  $30 \text{ g kg}^{-1}$ , at least in late summer, and river  
873 water fraction would be closer to 20 % (e.g., Bauch et al., 2011; Charette et al.,  
874 2020; Paffrath et al., 2021). The conditions observed after re-location closer to  
875 the North Pole (where the freshwater-rich part of the Transpolar Drift is often lo-  
876 cated), with surface salinities around  $29 \text{ g kg}^{-1}$  (Figure 4b), are more typical for  
877 the freshwater-rich part of the Transpolar Drift (e.g., Bauch et al., 2011; Charette  
878 et al., 2020). Provenance tracer data show that the river water component of the  
879 freshwater-rich part has a considerable proportion of Lena River water, while the  
880 lower river water fractions at the "edges" are mainly attributable to contributions  
881 from the Yenisei and Ob rivers (G Laukert, unpublished). This is consistent with  
882 a shorter advection time of Lena River water into the central Arctic Ocean, re-  
883 sulting in less mixing with ambient water, and suggests significant differences in  
884 biogeochemical water properties even within the river water-influenced part of the  
885 Transpolar Drift.

#### 886 8.1.2. Surface mixed layer depth

887 Peralta-Ferriz and Woodgate (2015) report estimates of the mixed layer depth for  
888 the whole Eurasian Basin, using 519 profiles in the time period 1979–2012. Based  
889 on monthly averages, they find a maximum mixed layer depth of 73 m in April,  
890 but also observed depths of  $>100 \text{ m}$  in winter and a minimum depth of 22 m in  
891 July/August. These ranges are similar to the conditions encountered during MO-  
892 SAiC, given the high internal variability of the mixed layer depth. Peralta-Ferriz  
893 and Woodgate (2015) also highlight that the Arctic mixed layer depth distribu-  
894 tion is patchy and they find a dominance of upper ocean stratification rather than  
895 wind or drift speed, on determining the local mixed layer depth in ice-covered  
896 situations. Throughout the MOSAiC drift, we also find the mixed layer depth to  
897 be strongly influenced by the surface salinity, which to first order sets the upper  
898 ocean stratification. In the presence of a surface salinity below  $30 \text{ g kg}^{-1}$ , the max-  
899 imum mixed layer depth is just over 20 m (Amundsen Basin, summer), whereas  
900 at a higher surface salinity of around  $32 \text{ g kg}^{-1}$ , the surface mixed layer can be as  
901 deep as 50 m. Deep ventilation, with a mixed layer depth of around 130 m, was  
902 observed only at a surface salinity greater than  $34.1 \text{ g kg}^{-1}$  (Nansen Basin). Win-  
903 ter deep ventilation has previously been observed (Polyakov et al., 2017) and was  
904 attributed to changes associated with Atlantification, e.g., weakened upper ocean  
905 stratification, higher turbulence and enhanced heat fluxes. MOSAiC data show  
906 that these conditions were present everywhere along the drift track in the Nansen

907 Basin. However, a similar disappearance of the halocline, related to a high surface  
908 salinity, has already been observed in the eastern Arctic Ocean in 1990's (Steele  
909 and Boyd, 1998) and was found to be transient (Boyd et al., 2002).

### 910 8.1.3. Halocline thickness and stratification

911 Based on 18,000 profiles of ocean temperature and salinity collected between  
912 1997–2008, Bourgain and Gascard (2011) assessed properties of the Arctic halo-  
913 cline. Similar to the variability encountered during MOSAiC, they found the  
914 strongest, i.e., most stratified, halocline layers close to the fresh water sources  
915 at the Siberian shelves. The weakest haloclines (together with the deepest mixed  
916 layers, down to 70 m) were found in the Western Nansen Basin, where we en-  
917 countered a deeper mixed layer and a complete absence of the halocline during  
918 MOSAiC. Bourgain and Gascard (2011) found the halocline in the Amundsen  
919 Basin to be very stable during their investigated time period, with no clear sea-  
920 sonal variability, but their data coverage in winter was sparse. During MOSAiC,  
921 we find an apparent seasonal signal, with a thicker ( $76 \pm 9$  m vs.  $50 \pm 11$  m) and  
922 more stratified ( $50 \pm 7 \times 10^{-5} \text{ s}^{-2}$  vs.  $28 \pm 8 \times 10^{-5} \text{ s}^{-2}$ ) halocline in summer,  
923 compared to the winter situation, which is attributed to a lower surface salinity in  
924 summer. However, while seasonal meltwater in the surface layer has an effect on  
925 the surface salinity, MOSAiC data indicate that it is the relative position within or  
926 outside the river-water influenced Transpolar Drift rather than seasonality, which  
927 sets the local surface salinity (see Section 4). Taking into account both seasons,  
928 the Amundsen basin halocline got thinner ( $55 \pm 14$  m vs.  $70 \pm 10$  m) but more  
929 stratified ( $32 \pm 12 \times 10^{-5} \text{ s}^{-2}$  vs.  $20 \pm 3 \times 10^{-5} \text{ s}^{-2}$ ) compared to the values  
930 reported in Bourgain and Gascard (2011). Given the strong spatial gradients in  
931 surface salinity in the Amundsen Basin and the still limited spatial coverage of  
932 data, these differences could reflect internal variability rather than trends.

### 933 8.1.4. Heat fluxes

934 Heat fluxes near the ice-ocean interface (at a depth of 3 m) exhibit low values dur-  
935 ing the MOSAiC winter and display significant day-to-day fluctuations. This pat-  
936 tern aligns with the findings of Meyer et al. (2017a) in the Nansen Basin during the  
937 N-ICE2015 winter (at 1 m depth). Moving into early spring, specifically in May,  
938 the heat fluxes recorded by the AOFB buoy reached levels of around  $5 \text{ W m}^{-2}$ ,  
939 a value that is consistent with the approximately  $10 \text{ W m}^{-2}$  reported by Meyer  
940 et al. (2017a) for the same month. In June, during the N-ICE2015 campaign, the  
941 fluxes ranged between  $10\text{--}50 \text{ W m}^{-2}$ , reaching peaks exceeding  $300 \text{ W m}^{-2}$  dur-  
942 ing storms that caused upward mixing of warm subsurface waters. Unfortunately,

943 the MOSAiC data lacks shallow measurements from June onwards.

944 Heat fluxes across the halocline during MOSAiC are virtually zero, which is  
945 in line with previous findings (Fer, 2009), also from the SHEBA campaign in  
946 the Western Arctic (Shaw and Stanton, 2014). Also, the relatively low heat fluxes  
947 over the Atlantic Water thermocline found in Amundsen Basin match previously  
948 reported values in that region (Lenn et al., 2009; Schulz et al., 2021). The higher  
949 heat fluxes over the thermocline found in the Nansen Basin correspond to values  
950 of around  $3 \text{ W m}^{-2}$  found during N-ICE2015 (Meyer et al., 2017a) and elevated  
951 heat fluxes in the absence of a halocline, as observed in the Nansen Basin, have  
952 previously been reported (Steele and Boyd, 1998). Heat fluxes over the thermo-  
953 cline for June and July were generally confined to the range of  $2\text{--}5 \text{ W m}^{-2}$ ; much  
954 lower than during N-ICE2015. This is primarily attributed to the shallower warm  
955 Atlantic layer in the N-ICE2015 area compared to the MOSAiC location and the  
956 absence of storms during this period of the MOSAiC drift.

## 957 8.2. *Interdisciplinary implications*

958 The regional differences in physical hydrography encountered during the MO-  
959 SAiC drift have various implications for other Arctic subsystems. In the follow-  
960 ing, we discuss how the variability in physical properties along the MOSAiC drift  
961 might shape the distribution of nutrients and the carbonate system, bio-optical  
962 properties, the ecological structure across multiple trophic levels and sea ice and  
963 atmospheric processes.

### 964 8.2.1. Nutrient and carbonate system dynamics

965 Water masses, transport and turbulent mixing impact the distribution of nutrients,  
966 carbon and other geochemical tracers. Nutrient inventories in the surface waters  
967 differ regionally, with signals being potentially larger than the seasonal signals  
968 of biological uptake and remineralization (Juranek, 2022), particularly in basins  
969 with longer ice-cover duration where the residence time of tracers is increased  
970 due to accumulation in surface waters (Eveleth et al., 2014). Similarly, for vari-  
971 ous carbonate system components, such as dissolved inorganic carbon (DIC) and  
972 total alkalinity (TA), a strong positive correlation is usually found with salinity  
973 (Friis et al., 2003), indicating that the marine carbonate system is closely related  
974 to physical water mass properties.

975 Atlantic Water, residing at depths greater than 100 m, forms the largest source  
976 of nutrients in the Central Arctic Ocean and is an enormous reservoir of dissolved  
977 inorganic carbon (DIC), as organic matter from the sun-lit surface ocean eventu-

978 ally sinks and remineralizes. The transport of these nutrients and carbon up to the  
979 photic zone, where they can be utilized by primary producers, is strongly limited  
980 by the presence of the halocline, which acts as a barrier layer (e.g., Fer, 2009;  
981 Schulz et al., 2022a). When the halocline is absent and the mixed layer penetrates  
982 the Atlantic Water layer (Polyakov et al., 2017), ventilation can potentially create  
983 locally larger nutrient inventories at the start of the productive season and enhance  
984 the biological carbon drawdown (Juraneck, 2022). This is observed in the Nansen  
985 Basin (Section 4.2). Enhanced vertical nutrient transport might also occur when  
986 Atlantic Water resides high up in the water column (Yermak Plateau, Section 4.3).  
987 On the other hand, vertical mixing of deep DIC during ventilation or passing ed-  
988 dies, can partially offset biological CO<sub>2</sub> drawdown by increasing the partial pres-  
989 sure of CO<sub>2</sub> (pCO<sub>2</sub>) in the surface layer (Bates and Mathis, 2009; Lannuzel et al.,  
990 2020).

991 Among marine carbonate system components, the surface layer pCO<sub>2</sub> is often  
992 the point of focus in sea-air CO<sub>2</sub> exchange studies, as it determines whether the  
993 ocean is a sink or source of CO<sub>2</sub> to the atmosphere. The Arctic Ocean is generally  
994 considered to be a CO<sub>2</sub> sink, as surface layer pCO<sub>2</sub> is often undersaturated relative  
995 to the atmosphere (Tanhua et al., 2009; Schuster et al., 2013; Fransson et al., 2017;  
996 Rogge et al., 2023). Arctic Ocean pCO<sub>2</sub> undersaturation is driven by low seawater  
997 temperatures, sea ice meltwater input, biological CO<sub>2</sub> uptake during the summer  
998 and strong upper ocean stratification (Bates et al., 2006; Takahashi et al., 2009;  
999 Fransson et al., 2017). In addition to the variability in the Arctic Ocean's nutri-  
1000 ent content and capacity to absorb atmospheric pCO<sub>2</sub> driven by biogeochemical  
1001 and sea ice processes, physical processes also can lead to changes in the marine  
1002 nutrient and carbonate system on short time scales. For example, frontal regions  
1003 are associated with enhanced biological activity, leading to variability in uptake  
1004 and remineralization rates of nutrients across smaller hydrographic scales (Eveleth  
1005 et al., 2014). Tidal currents in regions where horizontal gradients of water masses  
1006 exist, e.g., between Yermak Plateau and Fram Strait, can also lead to rapid change  
1007 in the nutrient and carbonate system of the surface ocean on semidiurnal and di-  
1008 urnal time scales and cause polar waters to switch between a CO<sub>2</sub> sink and source  
1009 multiple times a day (Skogseth et al., 2013; Llanillo et al., 2019; Droste et al.,  
1010 2022).

### 1011 8.2.2. Optical properties

1012 The optical properties of the surface waters exhibit regional differences between  
1013 the basins, exemplified by the documented differences in CDOM concentrations,  
1014 with elevated concentration when in the Transpolar Drift (see Section 4.2). In Arc-

1015 tic waters, CDOM is an important factor of light attenuation in the water column  
1016 (e.g., Hill, 2008; Granskog et al., 2007; Pavlov et al., 2015) and varies regionally,  
1017 largely depending on the presence of river water. This divides the Eurasian basin  
1018 in bio-optical provinces (Gonçalves-Araujo et al., 2018), which can have an effect  
1019 on the light availability for primary producers (e.g., Pavlov et al., 2015), especially  
1020 in the absence of sea ice. Solar heating of the upper ocean is also affected by the  
1021 distribution of CDOM (Hill, 2008; Granskog et al., 2015) and could thus affect  
1022 sea ice melting across regimes.

### 1023 8.2.3. Ecology

1024 Regional variability in both the nutrient concentration and the optical regime can  
1025 induce structural changes to the microorganism community, with complex im-  
1026 plications for the carbon biogeochemistry. For example, increased vertical trans-  
1027 port of nutrients from the deep ventilation observed in the Nansen Basin could  
1028 lead to a shift from smaller to larger phytoplankton, while increased stratifica-  
1029 tion and warming leads to opposite trends (Li et al., 2009; Morán et al., 2010).  
1030 Additionally, hydrographic boundaries can act as physical barriers limiting dis-  
1031 persal, resulting in vertical and biogeographic differences in microbial diversity  
1032 and community structure among water masses and basins (Galand et al., 2010;  
1033 Han et al., 2015). During MOSAiC, unique upper water column microbial com-  
1034 munity compositions were indeed observed when crossing boundaries such as the  
1035 base of the mixed layer, or when drifting into and out of the Transpolar Drift as de-  
1036 scribed here (EJ Chamberlain, unpublished). A key driver in regional differences  
1037 in Arctic Ocean bacterial communities is the relative proportion of Atlantic water  
1038 influence, with species composition and ecological function, i.e., substrate utiliza-  
1039 tion, responding rapidly to changes in the environmental regime. This connection  
1040 makes the variability in water masses, for example the high relative proportion  
1041 of Atlantic water observed while crossing the Yermak Plateau, a key driver in  
1042 regional differences of microbial communities (Carter-Gates et al., 2020; Priest  
1043 et al., 2023). At higher trophic levels, larger boreal species such as fish or squid  
1044 can enter the Arctic Ocean within the Atlantic Water layer and appear to sur-  
1045 vive in parts of the central Arctic. During MOSAiC, healthy Atlantic cod were  
1046 found in the Amundsen Basin, where a deep scattering layer indicates the pres-  
1047 ence of living organisms as food supply (Snoeijs-Leijonmalm et al., 2022). In the  
1048 Nansen Basin, this deep scattering layer was absent and fish and squid abundance  
1049 decreased. The inflow region of young Atlantic Water near Yermak Plateau, on  
1050 the other hand, was characterized by large aggregations of Atlantic fish species  
1051 (Snoeijs-Leijonmalm et al., 2022).

#### 1052 8.2.4. Sea ice and atmosphere

1053 Oceanic heat, when reaching the surface, has an effect on sea ice growth and  
1054 melt. During MOSAiC, the sea ice basal growth was found to transition from a  
1055 rapid to a slower growth rate, when drifting from Amundsen Basin to Nansen  
1056 Basin (Lei et al., 2022). This change in basal growth rate might be, to some ex-  
1057 tent, related to the greater vertical heat transport from the Atlantic Water layer in  
1058 the Nansen Basin, associated with the ventilation conditions (i.e., absence of the  
1059 halocline, Polyakov et al., 2017). During the melt season, elevated ocean surface  
1060 temperatures contribute to sea ice melt and small vertical gradients in upper ocean  
1061 temperature might set different melt rates at, e.g., ridge keels (Salganik et al.,  
1062 2023b). The presence of shallow, strongly stratified meltwater layers also affects  
1063 the sea-ice melt rates (Salganik et al., 2023a; Smith et al., 2023). Indirectly, even  
1064 atmospheric conditions might be influenced by surface ocean conditions, by af-  
1065 fecting the emission of marine aerosol precursors that play an important role in,  
1066 e.g., cloud formation (Schmale et al., 2021).

### 1067 9. Summary and outlook

1068 For this study, we compiled a quality-controlled dataset of temperature and salin-  
1069 ity profiles and derived parameters, with the best available temporal coverage  
1070 along the whole MOSAiC drift across the Eurasian basin in 2019–2020. De-  
1071 rived core parameters based on this dataset (supplemental Table S1, Schulz et al.,  
1072 2023b; Mieruch, 2023) can be used for interdisciplinary studies aiming to under-  
1073 stand interactions between ocean physical properties and a large range of other  
1074 measurements conducted during MOSAiC. We find that from an ocean perspec-  
1075 tive, MOSAiC was rather a transect across the Eurasian basin than a time series  
1076 primarily reflecting a seasonal evolution. Considerable gradients in the surface  
1077 waters are present, related to the MOSAiC ice camp drifting into and out of the  
1078 river water influenced Transpolar Drift in the Amundsen Basin. In the Nansen  
1079 Basin, high surface salinity and the associated absence of the halocline allows for  
1080 a more direct connection and enhanced exchange between the surface and deeper  
1081 waters of Atlantic origin. Further south, above Yermak Plateau and in the Fram  
1082 Strait, oceanic conditions were more dynamic, with a pronounced regime shift  
1083 back into surface waters with a high fraction of terrestrial water when leaving  
1084 Yermak Plateau. This spatial variability likely entails large implications for the  
1085 Arctic Ocean biogeochemistry, ecology and even sea ice and atmospheric condi-  
1086 tions.

1087 The large regional variability encountered during the drift already illustrates

1088 that MOSAiC results are not representative of the entire Arctic Ocean. Conditions  
1089 in the Eurasian deep basins are substantially different from the Amerasian Basin,  
1090 where the Beaufort Gyre accumulates large amounts of fresh water and Pacific  
1091 Water is commonly present in the upper water column. Conditions in the basins  
1092 also deviate from the more variable and energetic continental shelf and slope re-  
1093 gions. Furthermore, the observed strong dependence of ocean conditions on the  
1094 Transpolar Drift pathway, setting surface salinity, stratification and vertical trans-  
1095 port illustrates that a slight deviation in the ice drift path could have restricted  
1096 the range of sampled conditions. For example, if the drift track had not crossed  
1097 Gakkel Ridge and would have stayed within the cross-Arctic transport pathway  
1098 of Siberian freshwater, MOSAiC would have missed the ventilation conditions in  
1099 the Nansen Basin. The pathway of the Transpolar Drift depends on large-scale  
1100 atmospheric forcing and varies on interannual to decadal timescales (Polyakov  
1101 et al., 2023). In the period 2007–2021, a positive Arctic Dipole, i.e., relatively  
1102 higher sea level pressure over the Beaufort Sea and Canadian Archipelago and  
1103 lower sea level pressure over the Siberian Arctic, reinforced both the Beaufort  
1104 Gyre and shifted the Transpolar Drift path from the Amerasian Basin toward the  
1105 Lomonosov Ridge. Fresh water of Siberian origin accumulated in the Beaufort  
1106 Gyre, leading to a stronger salinity stratification in the Amerasian Basin, and a  
1107 weaker stratification in the Eurasian Basin. The underlying atmospheric forcing  
1108 changes on a timescale of approximately 15 years, and superimposes on climatic  
1109 trends such as warming Atlantic water and altered freshwater dynamics. For in-  
1110 stance, the less pronounced summer sea ice decline since 2007 might originate  
1111 from reduced ocean heat transport in the presence of stronger stratification in the  
1112 Amerasian Basin created by the positive Arctic Dipole (Polyakov et al., 2023).  
1113 The representativeness of MOSAiC results of the annual cycle and for other parts  
1114 of the Arctic, especially for the biogeochemical and ecological system needs to be  
1115 assessed with more observations. Nevertheless, the MOSAiC data will provide an  
1116 important benchmark for detecting future changes in the Eurasian basin.

1117 Future research efforts aiming to monitor climatic trends in the Arctic Ocean  
1118 need to account for this large interannual and regional variability, which ideally  
1119 requires long time series from stationary moorings and repeated sections/stations,  
1120 as well as wide temporal and spatial coverage by autonomous drifting buoys and  
1121 floats. Numerical models will be necessary to extrapolate and upscale observa-  
1122 tional data, by identifying the spatial extent of distinct oceanographic regimes  
1123 (e.g., ventilation conditions in the absence of a halocline (Polyakov et al., 2017)  
1124 as observed in the Nansen Basin) in response to seasonal and atmospheric forcing,  
1125 and to conduct process studies to isolate the respective effect of individual driving



1126 mechanisms for ocean variability. The strength of MOSAiC lies in its multidis-  
1127 ciplinary approach. MOSAiC observed key parameters simultaneously, including  
1128 atmospheric forcing, sea ice and ocean conditions, as well as ocean biogeochem-  
1129 istry and ecology at high temporal sampling frequency and on a range of scales  
1130 from manned measurements at the central floe, autonomous platforms in the sur-  
1131 rounding area to remote sensing by aircrafts and satellites. This strategy provides  
1132 unprecedented means to determine connections within the coupled Arctic system  
1133 on multiple timescales. Despite the challenges in data interpretation arising from  
1134 the overlapping timescales and the superposition of spatial and temporal signals  
1135 inherent to a drift campaign, it is the large variability of conditions observed dur-  
1136 ing MOSAiC that helps us to better understand processes and connections across  
1137 the coupled system over timescales from hours to months. MOSAiC data also pro-  
1138 vides an unprecedented opportunity for the scientific community to improve the  
1139 ocean and climate models pivotal to Arctic and Earth system research. However,  
1140 achieving this goal requires dedicated time, effective communication between ob-  
1141 servational and modeling communities, and adequate funding.

1142 One final aspect we would like to highlight about the value of MOSAiC for the  
1143 polar and climate research community are the countless fruitful scientific collabo-  
1144 rations that have been established as a result of this unique experiment. Despite or  
1145 perhaps because of the complexity of and challenges encountered during the cam-  
1146 paign, MOSAiC has created a striving community that has been working together  
1147 across disciplines to interpret the collected data, involving an increasing number  
1148 of early career scientists. Many of the collaborations and partnerships between the  
1149 international partners have been maintained, and even been strengthened and ex-  
1150 panded. The project serves as an example of how to foster scientific collaboration  
1151 and unleash the scientific spirit of a research community. In the end, the true value  
1152 of MOSAiC may likely be found beyond the experiment itself.

### 1153 Data accessibility statement

1154 All datasets used in this study are publicly available, in compliance with the MO-  
1155 SAiC data policy. In addition, we published a daily average dataset based on the  
1156 2,434 temperature and salinity profiles, as outlined in the supplemental material  
1157 Text S1, and derived parameters, as listed in Table S1 in the supplementary mate-  
1158 rial, in netCDF format (Schulz et al., 2023b). We also created webODV compliant  
1159 data files and views (Mieruch, 2023), from which subsets of data can easily be ex-  
1160 tracted. We strongly advise that future studies using the data presented here also  
1161 cite the respective original datasets listed below.

1162 CO1 GPS buoy: Nicolaus et al. (2021); CTD *Polarstern*: Tippenhauer et al.  
1163 (2023b,c); Ocean City CTD: Tippenhauer et al. (2023a,d); MSS: Schulz et al.  
1164 (2023c); ITPs (including CDOM data): Toole and Krishfield (2016); PG buoy O4:  
1165 Hoppmann et al. (2022); thermosalinograph: Rex et al. (2021a); Haas et al. (2021);  
1166 Kanzow et al. (2021); Rex et al. (2021b,c); ADCP: Baumann et al. (2021).

## 1167 Author Contributions

1168 Contributed to conception and design: KS, ZK, CJMH, EC, MM, IF, CH, MAG.

1169 Contributed to acquisition of data: KS, ZK, MM, DB, CJMH, ESD, MH, EC,  
1170 GL, TS, IF, CH, SK, TB, ST, MAG.

1171 Contributed to analysis and interpretation of data: KS, ZK, MM, DB, CJMH,  
1172 ESD, EC, GL, TS, AQ, IF, CH, SK, MV, MAG.

1173 Drafted and/or revised this article: All authors.

1174 Approved the submitted version for publication: All authors.

## 1175 Acknowledgements

1176 Data used in this manuscript were produced as part of the international Multi-  
1177 disciplinary drifting Observatory for the Study of the Arctic Climate (MOSAiC)  
1178 project with the tag MOSAiC20192020 and the Project.ID: AWI\_PS122\_00. The  
1179 Ice-Tethered Profiler data were collected and made available by the Ice-Tethered  
1180 Profiler Program (Toole et al., 2011; Krishfield et al., 2008) based at the Woods  
1181 Hole Oceanographic Institution (<https://www2.whoi.edu/site/itp/>). We thank all  
1182 persons involved in the expedition of the Research Vessel *Polarstern* (Knust,  
1183 2017) during MOSAiC in 2019–2020 as listed in the MOSAiC extended acknowl-  
1184 edgment Nixdorf et al. (2021). We especially thank everyone involved in the dis-  
1185 cussion during the Second MOSAiC Science Conference in Boulder, Colorado,  
1186 which motivated this study. We would also like to thank Daniela Ransby (Pan-  
1187 gaea) and Christopher Kracha (Arctic Data Center) for their great support with  
1188 the data publications.

## 1189 Funding

1190 Financial support for KS was available through the German (BMBF) and UK  
1191 (NERC) funded PEANUTS-project (grant number 03F0804A) and the NSF  
1192 funded projects NSF-AccelNet-2020387 and OPP-1936506. ZK, TB and IF re-  
1193 ceived funding through the AROMA (Arctic Ocean mixing processes and ver-  
1194 tical fluxes of energy and matter) project by the Research Council of Norway  
1195 (grant no 294396). ZK received funding from the Research Council of Norway

1196 through project BREATHE (grant no 325405). MM and MAG were supported  
1197 by funding from the European Union's Horizon 2020 research and innovation  
1198 programme under grant agreement No 101003826 via project CRiceS (Climate  
1199 Relevant interactions and feedbacks: the key role of sea ice and Snow in the polar  
1200 and global climate system) and the Research Council of Norway through project  
1201 HAVOC (grant no 280292). MAG also acknowledges support from the Hanse-  
1202 Wissenschaftskolleg Institute of Advanced Study (Delmenhorst, Germany). MV  
1203 was supported through the Changing Arctic Ocean (CAO) program, jointly funded  
1204 by the UKRI Natural Environment Research Council (NERC) and the BMBF,  
1205 project Advective Pathways of nutrients and key Ecological substances in the  
1206 ARctic (APEAR) grants NE/R012865/1, NE/R012865/2 and #03V01461. SK and  
1207 CH were supported by the Swedish Research Council (grant 2018-03859 awarded  
1208 to CH); participation of SK to MOSAiC was supported by the Swedish Research  
1209 Polar Secretariat. ESD was supported by the European Union's Horizon 2020  
1210 research and innovation programme under grant agreement no. 821001; partici-  
1211 pation of ESD on MOSAiC was supported by the Natural Environment Research  
1212 Council (NERC) through the EnvEast Doctoral Training Partnership (grant no.  
1213 NE/L002582/1) and the UK Department for Business, Energy and Industrial Strat-  
1214 egy (BEIS) through the UK Arctic Office. TS and the AOFB measurements are  
1215 funded by NSF OPP-1723400. GL also gratefully acknowledges financial support  
1216 from the Ocean Frontier Institute, supported by a Canada First Research Excel-  
1217 lence Fund award (grant no. 39291), and from the European Union's Horizon 2020  
1218 research and innovation program under a Marie Skłodowska-Curie Postdoctoral  
1219 Global Fellowship award (grant no. 101023769).

## 1220 Competing interests

1221 All authors declare that they have no competing interests.

## 1222 References

- 1223 Arrigo, KR, van Dijken, GL. 2015. Continued increases in Arctic Ocean  
1224 primary production. *Progress in Oceanography* **136**: 60–70. doi:  
1225 <https://doi.org/10.1016/j.pocean.2015.05.002>.
- 1226 Baker, MA, Gibson, CH. 1987. Sampling turbulence in the stratified  
1227 ocean: Statistical consequences of strong intermittency. *Journal of Phys-  
1228 ical Oceanography* **17**(10): 1817–1836. doi:[https://doi.org/10.1175/1520-  
1229 0485\(1987\)017<1817:STITSO>2.0.CO;2](https://doi.org/10.1175/1520-0485(1987)017<1817:STITSO>2.0.CO;2).
- 1230 Bates, N, Mathis, J. 2009. The Arctic Ocean marine carbon cycle: evaluation  
1231 of air-sea CO<sub>2</sub> exchanges, ocean acidification impacts and potential feed-  
1232 backs. *Biogeosciences* **6**(11): 2433–2459. doi:[https://doi.org/10.5194/bg-6-  
1233 2433-2009](https://doi.org/10.5194/bg-6-2433-2009).
- 1234 Bates, NR, Moran, SB, Hansell, DA, Mathis, JT. 2006. An increasing CO<sub>2</sub> sink in  
1235 the Arctic Ocean due to sea-ice loss. *Geophysical Research Letters* **33**(23).  
1236 doi:<https://doi.org/10.1029/2006GL027028>.
- 1237 Bauch, D, Cherniavskaia, E, Timokhov, L. 2016. Shelf basin exchange along the  
1238 Siberian continental margin: Modification of Atlantic Water and Lower Halo-  
1239 cline Water. *Deep Sea Research Part I: Oceanographic Research Papers* **115**:  
1240 188–198. doi:[10.1016/j.dsr.2016.06.008](https://doi.org/10.1016/j.dsr.2016.06.008).
- 1241 Bauch, D, van der Loeff, MR, Andersen, N, Torres-Valdes, S, Bakker, K, Abra-  
1242 hamsen, EP. 2011. Origin of freshwater and polynya water in the Arctic  
1243 Ocean halocline in summer 2007. *Progress in Oceanography* **91**(4): 482–  
1244 495. doi:<https://doi.org/10.1016/j.pocean.2011.07.017>.
- 1245 Baumann, T, Fer, I, Bryhni, H, Peterson, AK, Allerholt, J, Fang, YC, Hoppmann,  
1246 M, Karam, S, Koenig, Z, Kong, B, Mohrholz, V, Muilwijk, M, Schaffer, J,  
1247 Schulz, K, Sukhikh, N, Tippenhauer, S. 2021. Under-ice current measure-  
1248 ments during MOSAiC from a 75 kHz acoustic Doppler profiler. PANGAEA.  
1249 doi:<https://doi.org/10.1594/PANGAEA.934792>.
- 1250 Bouffard, D, Boegman, L. 2013. A diapycnal diffusivity model for stratified en-  
1251 vironmental flows. *Dynamics of Atmospheres and Oceans* **61**: 14–34. doi:  
1252 <https://doi.org/10.1016/j.dynatmoce.2013.02.002>.
- 1253 Bourgain, P, Gascard, JC. 2011. The Arctic Ocean halocline and its interannual  
1254 variability from 1997 to 2008. *Deep Sea Research Part I: Oceanographic Re-  
1255 search Papers* **58**(7): 745–756. doi:<https://doi.org/10.1016/j.dsr.2011.05.001>.
- 1256 Boyd, TJ, Steele, M, Muench, RD, Gunn, JT. 2002. Partial recovery of the  
1257 Arctic Ocean halocline. *Geophysical Research Letters* **29**(14): 2–1. doi:  
1258 <https://doi.org/10.1029/2001GL014047>.

- 1259 Boyer, TP, Garcia, HE, Locarnini, RA, Zweng, MM, Mishonov, AV, Reagan,  
1260 JR, Weathers, KA, Baranova, OK, Seidov, D, Smolyar, IV. 2018. World  
1261 Ocean Atlas 2018. *NOAA National Centers for Environmental Information*  
1262 <https://www.ncei.noaa.gov/archive/accession/NCEI-WOA18>.
- 1263 Carranza, MM, Gille, ST, Franks, PJ, Johnson, KS, Pinkel, R, Girton, JB.  
1264 2018. When mixed layers are not mixed. Storm-driven mixing and  
1265 bio-optical vertical gradients in mixed layers of the Southern Ocean.  
1266 *Journal of Geophysical Research: Oceans* **123**(10): 7264–7289. doi:  
1267 <https://doi.org/10.1029/2018JC014416>.
- 1268 Carter-Gates, M, Balestreri, C, Thorpe, SE, Cottier, F, Baylay, A, Bibby, TS,  
1269 Moore, CM, Schroeder, DC. 2020. Implications of increasing Atlantic in-  
1270 fluence for Arctic microbial community structure. *Scientific reports* **10**(1):  
1271 19262. doi:<https://doi.org/10.1038/s41598-020-76293-x>.
- 1272 Charette, MA, Kipp, LE, Jensen, LT, Dabrowski, JS, Whitmore, LM, Fitzsim-  
1273 mons, JN, Williford, T, Ulfso, A, Jones, E, Bundy, RM, Vivancos, SM,  
1274 Pahnke, K, John, SG, Xiang, Y, Hatta, M, Petrova, MV, Heimbürger-  
1275 Boavida, L, Bauch, D, Newton, R, Pasqualini, A, Agather, AM, Amon,  
1276 RMW, Anderson, RF, Andersson, PS, Benner, R, Bowman, KL, Edwards,  
1277 RL, Gdaniec, S, Gerringa, LJA, González, AG, Granskog, M, Haley, B,  
1278 Hammerschmidt, CR, Hansell, DA, Henderson, PB, Kadko, DC, Kaiser, K,  
1279 Laan, P, Lam, PJ, Lamborg, CH, Levier, M, Li, X, Margolin, AR, Mea-  
1280 sures, C, Middag, R, Millero, FJ, Moore, WS, Paffrath, R, Planquette, H,  
1281 Rabe, B, Reader, H, Rember, R, Rijkenberg, MJA, Roy-Barman, M, Rut-  
1282 ters van der Loeff, M, Saito, M, Schauer, U, Schlosser, P, Sherrell, RM,  
1283 Shiller, AM, Slagter, H, Sonke, JE, Stedmon, C, Woosley, RJ, Valk, O, Ooi-  
1284 jen, J, Zhang, R. 2020. The Transpolar Drift as a Source of Riverine and  
1285 Shelf-Derived Trace Elements to the Central Arctic Ocean. *Journal of Geo-*  
1286 *physical Research: Oceans* **125**(5): e2019JC015920. ISSN 2169-9275. doi:  
1287 <https://doi.org/10.1029/2019JC015920>.
- 1288 Dossier, H, Chanona, M, Waterman, S, Shibley, N, Timmermans, ML. 2021.  
1289 Changes in internal wave-driven mixing across the Arctic Ocean: Finescale  
1290 estimates from an 18-year pan-Arctic record. *Geophysical Research Letters*  
1291 **48**(8): e2020GL091747. doi:<https://doi.org/10.1029/2020GL091747>.
- 1292 Droste, ES, Hoppema, M, González-Dávila, M, Santana-Casiano, JM, Queste,  
1293 BY, Dall'Olmo, G, Venables, HJ, Rohardt, G, Ossebaar, S, Schuller, D, et al.  
1294 2022. The influence of tides on the marine carbonate chemistry of a coastal  
1295 polynya in the south-eastern Weddell Sea. *Ocean Science* **18**(5): 1293–1320.  
1296 doi:<https://doi.org/10.5194/os-18-1293-2022>.

- 1297 Erofeeva, S, Egbert, G. 2020. Arc5km2018: Arctic Ocean Inverse Tide  
1298 Model on a 5 kilometer grid, 2018. Dataset. Arctic Data Center. doi:  
1299 10.18739/A21R6N14K.
- 1300 Eveleth, R, Timmermans, ML, Cassar, N. 2014. Physical and biological controls  
1301 on oxygen saturation variability in the upper Arctic Ocean. *Journal of Geo-*  
1302 *physical Research: Oceans* **119**: 7420–7432. doi:10.1002/2014JC009816.
- 1303 Fer, I. 2009. Weak vertical diffusion allows maintenance of cold halocline in the  
1304 central Arctic. *Atmospheric and Oceanic Science Letters* **2**(3): 148–152. doi:  
1305 <https://doi.org/10.1080/16742834.2009.11446789>.
- 1306 Fer, I, Baumann, TM, Koenig, Z, Muilwijk, M, Tippenhauer, S. 2022. Upper-  
1307 Ocean Turbulence Structure and Ocean-Ice Drag Coefficient Estimates  
1308 Using an Ascending Microstructure Profiler During the MOSAiC Drift.  
1309 *Journal of Geophysical Research: Oceans* **127**(9): e2022JC018751. doi:  
1310 <https://doi.org/10.1029/2022JC018751>.
- 1311 Fer, I, Müller, M, Peterson, A. 2015. Tidal forcing, energetics, and mixing near  
1312 the Yermak Plateau. *Ocean Sci* **11**: 287–304. doi:[https://doi.org/10.5194/os-](https://doi.org/10.5194/os-11-287-2015)  
1313 [11-287-2015](https://doi.org/10.5194/os-11-287-2015).
- 1314 Fine, EC, Cole, ST. 2022. Decadal Observations of Internal Wave En-  
1315 ergy, Shear, and Mixing in the Western Arctic Ocean. *Journal*  
1316 *of Geophysical Research: Oceans* **127**(5): e2021JC018056. doi:  
1317 <https://doi.org/10.1029/2021JC018056>.
- 1318 Fong, AA, et al. 2023. Overview of the MOSAiC expedition: Ecosystem  
1319 [preprint]. *Earth arXiv* doi:<https://doi.org/10.31223/X5P091>.
- 1320 Forget, G, Campin, JM, Heimbach, P, Hill, CN, Ponte, RM, Wunsch, C. 2015.  
1321 ECCO version 4: An integrated framework for non-linear inverse mod-  
1322 eling and global ocean state estimation. *Geoscientific Model Develop-*  
1323 *ment* **8**(10): 3071–3104. ISSN 1991-9603. doi:[https://doi.org/10.5194/gmd-](https://doi.org/10.5194/gmd-8-3071-2015)  
1324 [8-3071-2015](https://doi.org/10.5194/gmd-8-3071-2015).
- 1325 Fouest, VL, Babin, M, Tremblay, JÉ. 2013. The fate of riverine nutrients on Arctic  
1326 shelves. *Biogeosciences* **10**(6): 3661–3677. doi:[https://doi.org/10.5194/bg-](https://doi.org/10.5194/bg-10-3661-2013)  
1327 [10-3661-2013](https://doi.org/10.5194/bg-10-3661-2013).
- 1328 Fransson, A, Chierici, M, Skjelvan, I, Olsen, A, Assmy, P, Peterson, AK,  
1329 Spreen, G, Ward, B. 2017. Effects of sea-ice and biogeochemical pro-  
1330 cesses and storms on under-ice water fCO<sub>2</sub> during the winter-spring  
1331 transition in the high Arctic Ocean: Implications for sea-air CO<sub>2</sub>  
1332 fluxes. *Journal of Geophysical Research: Oceans* **122**(7): 5566–5587. doi:  
1333 <https://doi.org/10.1002/2016JC012478>.
- 1334 Friis, K, Körtzinger, A, Wallace, DW. 2003. The salinity normalization of marine

- 1335 inorganic carbon chemistry data. *Geophysical Research Letters* **30**(2). doi:  
1336 <https://doi.org/10.1029/2002GL015898>.
- 1337 Galand, PE, Potvin, M, Casamayor, EO, Lovejoy, C. 2010. Hydrography shapes  
1338 bacterial biogeography of the deep Arctic Ocean. *The ISME journal* **4**(4):  
1339 564–576. doi:<https://doi.org/10.1038/ismej.2009.134>.
- 1340 Gibson, GA, Elliot, S, Clement Kinney, J, Piliouras, A, Jeffery, N.  
1341 2022. Assessing the potential impact of river chemistry on arc-  
1342 tic coastal production. *Frontiers in Marine Science* **9**: 738363. doi:  
1343 <https://doi.org/10.3389/fmars.2022.738363>.
- 1344 Gonçalves-Araujo, R, Granskog, MA, Bracher, A, Azetsu-Scott, K, Dodd, PA,  
1345 Stedmon, CA. 2016. Using fluorescent dissolved organic matter to trace and  
1346 distinguish the origin of Arctic surface waters. *Scientific Reports* **6**(1): 33978.  
1347 ISSN 2045-2322. doi:<https://doi.org/10.1038/srep33978>.
- 1348 Gonçalves-Araujo, R, Rabe, B, Peeken, I, Bracher, A. 2018. High colored dis-  
1349 solved organic matter (CDOM) absorption in surface waters of the central-  
1350 eastern Arctic Ocean: Implications for biogeochemistry and ocean color al-  
1351 gorithms. *PLOS ONE* **13**: e0190838. doi:10.1371/journal.pone.0190838.
- 1352 Gordó-Vilaseca, C, Stephenson, F, Coll, M, Lavin, C, Costello, MJ. 2023. Three  
1353 decades of increasing fish biodiversity across the northeast Atlantic and the  
1354 Arctic Ocean. *Proceedings of the National Academy of Sciences* **120**(4):  
1355 e2120869120. doi:<https://doi.org/10.1073/pnas.2120869120>.
- 1356 Granskog, MA, Macdonald, RW, Mundy, CJ, Barber, DG. 2007. Distribution,  
1357 characteristics and potential impacts of chromophoric dissolved organic mat-  
1358 ter (CDOM) in Hudson Strait and Hudson Bay, Canada. *Continental Shelf*  
1359 *Research* **27**: 2032–2050. doi:<https://doi.org/10.1016/j.csr.2007.05.001>.
- 1360 Granskog, MA, Pavlov, AK, Sagan, S, Kowalczyk, P, Raczkowska, A, Stedmon,  
1361 CA. 2015. Effect of sea-ice melt on inherent optical properties and verti-  
1362 cal distribution of solar radiant heating in Arctic surface waters. *Journal of*  
1363 *Geophysical Research: Oceans* **120**(10): 7028–7039. ISSN 2169-9275. doi:  
1364 [10.1002/2015JC011087](https://doi.org/10.1002/2015JC011087).
- 1365 Guthrie, J, Fer, I, Morison, J. 2017. Thermohaline Staircases in the  
1366 Amundsen Basin: possible disruption by shear and mixing. *Jour-  
1367 nal of Geophysical Research: Oceans* **122**: 7767– 7782. doi:  
1368 <https://doi.org/10.1002/2017JC012993>.
- 1369 Haas, C, Hoppmann, M, Tippenhauer, S, Rohardt, G. 2021. Continuous thermos-  
1370 alinograph oceanography along RV POLARSTERN cruise track PS122/2.  
1371 PANGAEA. doi:<https://doi.org/10.1594/PANGAEA.930024>.
- 1372 Han, D, Ha, HK, Hwang, CY, Lee, BY, Hur, HG, Lee, YK. 2015. Bacterial

- 1373 communities along stratified water columns at the Chukchi Borderland in  
1374 the western Arctic Ocean. *Deep Sea Research Part II: Topical Studies in*  
1375 *Oceanography* **120**: 52–60. doi:<https://doi.org/10.1016/j.dsr2.2015.01.018>.
- 1376 Heuzé, C, Huhn, O, Walter, M, Sukhikh, N, Karam, S, Körtke, W, Vredenburg, M,  
1377 Bulsiewicz, K, Sültenfuß, J, Fang, YC, Mertens, C, Rabe, B, Tippenhauer, S,  
1378 Allerholt, J, He, H, Kuhlmeier, D, Kuznetsov, I, Mallet, M. 2023a. A year of  
1379 transient tracers chlorofluorocarbon 12 and sulfur hexafluoride, noble gases  
1380 helium and neon, and tritium in the Arctic Ocean from the MOSAiC expedi-  
1381 tion (2019-2020). *Earth System Science Data Discussions* doi:10.5194/essd-  
1382 2023-232.
- 1383 Heuzé, C, Zanowski, H, Karam, S, Muilwijk, M. 2023b. The deep Arctic Ocean  
1384 and Fram Strait in CMIP6 models. *Journal of Climate* **36**(8): 2551–2584.  
1385 doi:<https://doi.org/10.1175/JCLI-D-22-0194.1>.
- 1386 Hill, VJ. 2008. Impacts of chromophoric dissolved organic material on surface  
1387 ocean heating in the Chukchi Sea. *Journal of Geophysical Research* **113**:  
1388 C07024. doi:10.1029/2007JC004119.
- 1389 Hoppmann, M, Kuznetsov, I, Fang, YC, Rabe, B. 2022. Processed data of CTD  
1390 buoys 2019O1 to 2019O8 as part of the MOSAiC Distributed Network. PAN-  
1391 GAEA. doi:<https://doi.org/10.1594/PANGAEA.940320>.
- 1392 Jakobsson, M, Mayer, LA, Bringsparr, C, Castro, CF, Mohammad, R, Johnson,  
1393 P, Ketter, T, Accettella, D, Amblas, D, An, L, et al. 2020. The international  
1394 bathymetric chart of the Arctic Ocean version 4.0. *Scientific data* **7**(1): 176.  
1395 doi:<https://doi.org/10.1038/s41597-020-0520-9>.
- 1396 Janout, MA, Hölemann, J, Laukert, G, Smirnov, A, Krumpen, T, Bauch, D,  
1397 Timokhov, L. 2020. On the variability of stratification in the freshwater-  
1398 influenced Laptev Sea Region. *Frontiers in Marine Science* **7**: 543489. doi:  
1399 <https://doi.org/10.3389/fmars.2020.543489>.
- 1400 Juranek, LW. 2022. Changing biogeochemistry of the Arctic Ocean. *Oceanogra-*  
1401 *phy* **35**(3/4): 144–155. doi:<https://doi.org/10.5670/oceanog.2022.120>.
- 1402 Kanzow, T, Hoppmann, M, Tippenhauer, S, Rohardt, G. 2021. Continuous  
1403 thermosalinograph oceanography along RV POLARSTERN cruise track  
1404 PS122/3. PANGAEA. doi:<https://doi.org/10.1594/PANGAEA.930026>.
- 1405 Karam, S, Heuzé, C, Hoppmann, M, de Steur, L. 2024. Con-  
1406 tinued warming of deep waters in Fram Strait. *EGU-*  
1407 *sphere* **2024**: 1–23. doi:10.5194/egusphere-2024-458.  
1408 <https://egusphere.copernicus.org/preprints/2024/egusphere-2024-458>
- 1409 Karam, S, Heuzé, C, Müller, V, Zheng, Y. 2023. Recirculation of Canada  
1410 Basin Deep Water in the Amundsen Basin, Arctic. *Journal of Physi-*



- 1411 *cal Oceanography* **53**(11): 2559 – 2574. doi:10.1175/JPO-D-22-0252.1.  
1412 <https://journals.ametsoc.org/view/journals/phoc/53/11/JPO-D-22-0252.1>.
- 1413 Karcher, M, Smith, JN, Kauker, F, Gerdes, R, Smethie, WM. 2012. Re-  
1414 cent changes in Arctic Ocean circulation revealed by iodine-129 observa-  
1415 tions and modeling. *Journal of Geophysical Research* **117**: C08007. doi:  
1416 10.1029/2011JC007513.
- 1417 Kawaguchi, Y, Koenig, Z, Nomura, D, Hoppmann, M, Inoue, J, Fang, YC,  
1418 Schulz, K, Gallagher, M, Katlein, C, Nicolaus, M, et al. 2022. Tur-  
1419 bulent mixing during late summer in the ice–ocean boundary layer  
1420 in the central Arctic Ocean: Results from the MOSAiC expedition.  
1421 *Journal of Geophysical Research: Oceans* **127**(8): e2021JC017975. doi:  
1422 <https://doi.org/10.1029/2021JC017975>.
- 1423 Kim, YH, Min, SK, Gillett, NP, Notz, D, Malinina, E. 2023. Observationally-  
1424 constrained projections of an ice-free Arctic even under a low emission sce-  
1425 nario. *Nature Communications* **14**. doi:[https://doi.org/10.1038/s41467-023-](https://doi.org/10.1038/s41467-023-38511-8)  
1426 [38511-8](https://doi.org/10.1038/s41467-023-38511-8).
- 1427 Knust, R. 2017. Polar research and supply vessel POLARSTERN operated by  
1428 the Alfred-Wegener-Institute. *Journal of Large-Scale Research Facilities* **3**:  
1429 A119. doi:<https://doi.org/10.17815/jlsrf-3-163>.
- 1430 Kong, X. 2022. *Molecular and optical characterization of dissolved*  
1431 *organic matter in the Central Arctic Ocean*. Phd thesis, Uni-  
1432 versity of Bremen, Dissertation, 2022, Bremen. 159 pages.  
1433 <https://suche.suub.uni-bremen.de/peid=B183177399>.
- 1434 Korhonen, M, Rudels, B, Marnela, M, Wisotzki, A, Zhao, J. 2013. Time and  
1435 space variability of freshwater content, heat content and seasonal ice melt  
1436 in the Arctic Ocean from 1991 to 2011. *Ocean Science* **9**(6): 1015–1055.  
1437 doi:<https://doi.org/10.5194/osd-9-2621-2012>.
- 1438 Krishfield, R, Toole, J, Proshutinsky, A, Timmermans, ML. 2008. Automated ice-  
1439 tethered profilers for seawater observations under pack ice in all seasons.  
1440 *Journal of Atmospheric and Oceanic Technology* **25**(11): 2091–2105. doi:  
1441 <https://doi.org/10.1175/2008JTECHO587.1>.
- 1442 Krumpen, T, Belter, HJ, Boetius, A, Damm, E, Haas, C, Hendricks, S, Nicolaus,  
1443 M, Nöthig, EM, Paul, S, Peeken, I, et al. 2019. Arctic warming interrupts the  
1444 Transpolar Drift and affects long-range transport of sea ice and ice-rafted  
1445 matter. *Scientific Reports* **9**(1): 5459. doi:[https://doi.org/10.1038/s41598-](https://doi.org/10.1038/s41598-019-41456-y)  
1446 [019-41456-y](https://doi.org/10.1038/s41598-019-41456-y).
- 1447 Kwok, R. 2018. Arctic sea ice thickness, volume, and multiyear ice coverage:  
1448 losses and coupled variability (1958–2018). *Environmental Research Letters*

- 1449 **13**(10): 105005. doi:<https://doi.org/10.1088/1748-9326/aae3ec>.
- 1450 Lannuzel, D, Tedesco, L, Van Leeuwe, M, Campbell, K, Flores, H, Delille, B,  
1451 Miller, L, Stefels, J, Assmy, P, Bowman, J, et al. 2020. The future of Arctic  
1452 sea-ice biogeochemistry and ice-associated ecosystems. *Nature Climate  
1453 Change* **10**(11): 983–992. doi:<https://doi.org/10.1038/s41558-020-00940-4>.
- 1454 Laukert, G, Frank, M, Bauch, D, Hathorne, EC, Rabe, B, von Appen, WJ, Weg-  
1455 ner, C, Zieringer, M, Kassens, H. 2017. Ocean circulation and freshwater  
1456 pathways in the Arctic Mediterranean based on a combined Nd isotope, REE  
1457 and oxygen isotope section across Fram Strait. *Geochimica et Cosmochimica  
1458 Acta* **202**: 285–309. doi:<https://doi.org/10.1016/j.gca.2016.12.028>.
- 1459 Laukert, G, Grasse, P, Novikhin, A, Povazhnyi, V, Doering, K, Hölemann, J,  
1460 Janout, M, Bauch, D, Kassens, H, Frank, M. 2022. Nutrient and silicon iso-  
1461 tope dynamics in the Laptev Sea and implications for nutrient availability in  
1462 the transpolar drift. *Global Biogeochemical Cycles* **36**(9): e2022GB007316.  
1463 doi:<https://doi.org/10.1029/2022GB007316>.
- 1464 Laukert, G, Makhotin, M, Petrova, MV, Frank, M, Hathorne, EC, Bauch,  
1465 D, Böning, P, Kassens, H. 2019. Water mass transformation in the Bar-  
1466 ents Sea inferred from radiogenic neodymium isotopes, rare earth ele-  
1467 ments and stable oxygen isotopes. *Chemical Geology* **511**: 416–430. doi:  
1468 <https://doi.org/10.1016/j.chemgeo.2018.10.002>.
- 1469 Lei, R, Cheng, B, Hoppmann, M, Zhang, F, Zuo, G, Hutchings, JK, Lin, L,  
1470 Lan, M, Wang, H, Regnery, J, et al. 2022. Seasonality and timing of  
1471 sea ice mass balance and heat fluxes in the Arctic transpolar drift dur-  
1472 ing 2019–2020. *Elementa Science of the Anthropocene* **10**(1): 000089. doi:  
1473 <https://doi.org/10.1525/elementa.2021.000089>.
- 1474 Lenn, YD, Wiles, P, Torres-Valdes, S, Abrahamsen, E, Rippeth, T, Simpson, J,  
1475 Bacon, S, Laxon, S, Polyakov, I, Ivanov, V, et al. 2009. Vertical mixing at  
1476 intermediate depths in the Arctic boundary current. *Geophysical Research  
1477 Letters* **36**(5). doi:<https://doi.org/10.1029/2008GL036792>.
- 1478 Li, WK, McLaughlin, FA, Lovejoy, C, Carmack, EC. 2009. Smallest algae  
1479 thrive as the Arctic Ocean freshens. *Science* **326**(5952): 539–539. doi:  
1480 [10.1126/science.1179798](https://doi.org/10.1126/science.1179798).
- 1481 Llanillo, P, Aiken, CM, Cordero, R, Damiani, A, Sepúlveda, E, Fernández-  
1482 Gómez, B. 2019. Oceanographic variability induced by tides, the in-  
1483 traseasonal cycle and warm subsurface water intrusions in Maxwell Bay,  
1484 King George Island (West-Antarctica). *Scientific reports* **9**(1): 18571. doi:  
1485 <https://doi.org/10.1038/s41598-019-54875-8>.
- 1486 Locarnini, R, Mishonov, A, Baranova, O, Boyer, T, Zweng, M, Garcia, H, Rea-

- 1487 gan, J, Seidov, D, Weathers, K, Paver, C, Smolyar, I. 2018. *World Ocean At-*  
1488 *las 2018, Volume 1: Temperature*. A. Mishonov Technical Ed.; NOAA Atlas  
1489 NESDIS 81.
- 1490 Marnela, M, Rudels, B, Goszczko, I, Beszczynska-Möller, A, Schauer, U. 2016.  
1491 Fram Strait and Greenland Sea transports, water masses, and water mass  
1492 transformations 1999–2010 (and beyond). *Journal of Geophysical Research:*  
1493 *Oceans* **121**(4): 2314–2346. doi:<https://doi.org/10.1002/2015JC011312>.
- 1494 McDougall, TJ, Barker, PM. 2011. Getting started with TEOS-10 and the Gibbs  
1495 Seawater (GSW) oceanographic toolbox. *SCOR/IAPSO WG* **127**: 1–28.
- 1496 McPhee, M. 2008. *Air-ice-ocean interaction: Turbulent ocean boundary layer ex-*  
1497 *change processes*. Springer Science & Business Media.
- 1498 Meyer, A, Fer, I, Sundfjord, A, Peterson, AK. 2017a. Mixing rates and  
1499 vertical heat fluxes north of Svalbard from Arctic winter to spring.  
1500 *Journal of Geophysical Research: Oceans* **122**(6): 4569–4586. doi:  
1501 <https://doi.org/10.1002/2016JC012441>.
- 1502 Meyer, A, Sundfjord, A, Fer, I, Provost, C, Villaciers Robineau, N, Koenig, Z,  
1503 Onarheim, IH, Smedsrud, LH, Duarte, P, Dodd, PA, et al. 2017b. Winter  
1504 to summer oceanographic observations in the Arctic Ocean north of Sval-  
1505 bard. *Journal of Geophysical Research: Oceans* **122**(8): 6218–6237. doi:  
1506 <https://doi.org/10.1002/2016JC012391>.
- 1507 Mieruch, S. 2023. smieruch/mosaic\_hydrographic\_core\_parameters:  
1508 Initial Release. Zenodo. doi:10.5281/zenodo.8304184.  
1509 <https://doi.org/10.5281/zenodo.8304184>.
- 1510 Mieruch, S, Schlitzer, R. 2023. smieruch/webodv: we-  
1511 bodv v1.0.0. Zenodo. doi:10.5281/zenodo.8241241.  
1512 <https://doi.org/10.5281/zenodo.8241241>.
- 1513 Morán, XAG, López-Urrutia, Á, Calvo-Díaz, A, Li, WK. 2010. Increasing im-  
1514 portance of small phytoplankton in a warmer ocean. *Global Change Biology*  
1515 **16**(3): 1137–1144. doi:<https://doi.org/10.1111/j.1365-2486.2009.01960.x>.
- 1516 Mysak, LA. 2001. Patterns of Arctic Circulation. *Science* **293**(5533): 1269–1270.  
1517 doi:DOI: 10.1126/science.1064217.
- 1518 Nguyen, AT, Pillar, H, Ocaña, V, Bigdeli, A, Smith, TA, Heimbach, P. 2021.  
1519 The Arctic Subpolar Gyre sTate Estimate: Description and Assessment  
1520 of a Data-Constrained, Dynamically Consistent Ocean-Sea Ice Estimate  
1521 for 2002–2017. *Journal of Advances in Modeling Earth Systems* **13**(5):  
1522 e2020MS002398. doi:<https://doi.org/10.1029/2020MS002398>.
- 1523 Nicolaus, M, Perovich, DK, Spreen, G, Granskog, MA, von Albedyll, L, An-  
1524 gelopoulos, M, Anhaus, P, Arndt, S, Belter, HJ, Bessonov, V, et al. 2022.

- 1525 Overview of the MOSAiC expedition: Snow and sea ice. *Elem Sci Anth*  
1526 **10**(1): 000046. doi:<https://doi.org/10.1525/elementa.2021.000046>.
- 1527 Nicolaus, M, Riemann-Campe, K, Bliss, A, Hutchings, JK, Granskog,  
1528 MA, Haas, C, Hoppmann, M, Kanzow, T, Krishfield, RA, Lei, R,  
1529 Rex, M, Li, T, Rabe, B. 2021. Drift trajectories of the main sites  
1530 of the Distributed Network of MOSAiC 2019/2020. PANGAEA. doi:  
1531 <https://doi.org/10.1594/PANGAEA.937204>.
- 1532 Nixdorf, U, Dethloff, K, Rex, M, Shupe, M, Sommerfeld, A, Perovich, DK,  
1533 Nicolaus, M, Heuzé, C, Rabe, B, Loose, B, Damm, E, Gradinger, R, Fong,  
1534 A, Maslowski, W, Rinke, A, Kwok, R, Spreen, G, Wendisch, M, Her-  
1535 ber, A, Hirsekorn, M, Mohaupt, V, Frickenhaus, S, Immerz, A, Weiss-  
1536 Tuidler, K, König, B, Mengedoht, D, Regnery, J, Gerchow, P, Ransby, D,  
1537 Krumpfen, T, Morgenstern, A, Haas, C, Kanzow, T, Rack, FR, Saitzev,  
1538 V, Sokolov, V, Makarov, A, Schwarze, S, Wunderlich, T, Wurr, K,  
1539 Boetius, A. 2021. MOSAiC Extended Acknowledgement. Zenodo. doi:  
1540 <https://doi.org/10.5281/zenodo.5541624>.
- 1541 Nomura, D, Kawaguchi, Y, Webb, AL, Li, Y, Dall’osto, M, Schmidt, K, Droste,  
1542 ES, Chamberlain, EJ, Kolabutin, N, Shimanchuk, E, et al. 2023. Meltwater  
1543 layer dynamics in a central Arctic lead: Effects of lead width, re-freezing, and  
1544 mixing during late summer. *Elementa: Science of the Anthropocene* **11**(1).  
1545 doi:<https://doi.org/10.1525/elementa.2022.00102>.
- 1546 Paffrath, R, Laukert, G, Bauch, D, Rutgers van der Loeff, M, Pahnke, K.  
1547 2021. Separating individual contributions of major Siberian rivers in the  
1548 Transpolar Drift of the Arctic Ocean. *Scientific Reports* **11**(1): 1–11. doi:  
1549 <https://doi.org/10.1038/s41598-021-86948-y>.
- 1550 Pavlov, AK, Granskog, MA, Stedmon, CA, Ivanov, BV, Hudson, SR, Falk-  
1551 Petersen, S. 2015. Contrasting optical properties of surface waters across the  
1552 Fram Strait and its potential biological implications. *Journal of Marine Sys-*  
1553 *tems* **143**: 62–72. ISSN 09247963. doi:10.1016/j.jmarsys.2014.11.001.
- 1554 Peralta-Ferriz, C, Woodgate, RA. 2015. Seasonal and interannual variabil-  
1555 ity of pan-Arctic surface mixed layer properties from 1979 to 2012  
1556 from hydrographic data, and the dominance of stratification for multiyear  
1557 mixed layer depth shoaling. *Progress in Oceanography* **134**: 19–53. doi:  
1558 <https://doi.org/10.1016/j.pocean.2014.12.005>.
- 1559 Perovich, D, Raphael, I, Moore, R, Clemens–Sewall, D, Lei, R, Sledd, A, Po-  
1560 lashenski, C. accepted. Sea ice heat and mass balance measurements from  
1561 four autonomous buoys during the MOSAiC drift campaign. *Elementa: Sci-*  
1562 *ence of the Anthropocene* .

- 1563 Polyakov, IV, Ingvaldsen, RB, Pnyushkov, AV, Bhatt, US, Francis, JA, Janout, M,  
1564 Kwok, R, Skagseth, Ø. 2023. Fluctuating Atlantic inflows modulate Arctic  
1565 atlantification. *Science* **381**(6661): 972–979. doi:10.1126/science.adh5158.
- 1566 Polyakov, IV, Pnyushkov, AV, Alkire, MB, Ashik, IM, Baumann, TM, Carmack,  
1567 EC, Goszczko, I, Guthrie, J, Ivanov, VV, Kanzow, T, et al. 2017. Greater role  
1568 for Atlantic inflows on sea-ice loss in the Eurasian Basin of the Arctic Ocean.  
1569 *Science* **356**(6335): 285–291. doi:https://doi.org/10.1126/science.aai8204.
- 1570 Polyakov, IV, Rippeth, TP, Fer, I, Alkire, MB, Baumann, TM, Carmack, EC, Ing-  
1571 valdsen, R, Ivanov, VV, Janout, M, Lind, S, et al. 2020a. Weakening of cold  
1572 halocline layer exposes sea ice to oceanic heat in the eastern Arctic Ocean.  
1573 *Journal of Climate* **33**(18): 8107–8123. doi:https://doi.org/10.1175/JCLI-D-  
1574 19-0976.1.
- 1575 Polyakov, IV, Rippeth, TP, Fer, I, Baumann, TM, Carmack, EC, Ivanov,  
1576 VV, Janout, M, Padman, L, Pnyushkov, AV, Rember, R. 2020b. In-  
1577 tensification of near-surface currents and shear in the Eastern Arc-  
1578 tic Ocean. *Geophysical Research Letters* **47**(16): e2020GL089469. doi:  
1579 https://doi.org/10.1029/2020GL089469.
- 1580 Priest, T, von Appen, WJ, Oldenburg, E, Popa, O, Torres-Valdés, S, Bien-  
1581 hold, C, Metfies, K, Boulton, W, Mock, T, Fuchs, BM, et al. 2023. At-  
1582 lantic water influx and sea-ice cover drive taxonomic and functional shifts  
1583 in Arctic marine bacterial communities. *The ISME Journal* pp. 1–14. doi:  
1584 https://doi.org/10.1038/s41396-023-01461-6.
- 1585 Rabe, B, Heuzé, C, Regnery, J, Aksenov, Y, Allerholt, J, Athanase, M, Bai, Y,  
1586 Basque, C, Bauch, D, Baumann, TM, Chen, D, Cole, ST, Craw, L, Davies,  
1587 A, Damm, E, Dethloff, K, Divine, DV, Doglioni, F, Ebert, F, Fang, YC, Fer, I,  
1588 Fong, AA, Gradinger, R, Granskog, MA, Graupner, R, Haas, C, He, H, He, Y,  
1589 Hoppmann, M, Janout, M, Kadko, D, Kanzow, T, Karam, S, Kawaguchi, Y,  
1590 Koenig, Z, Kong, B, Krishfield, RA, Krumpfen, T, Kuhlmeier, D, Kuznetsov, I,  
1591 Lan, M, Lei, R, Li, T, Torres-Valdés, S, Lin, L, Lin, L, Liu, H, Liu, N, Loose,  
1592 B, Ma, X, MacKay, R, Mallet, M, Mallett, RDC, Maslowski, W, Mertens,  
1593 C, Mohrholz, V, Muilwijk, M, Nicolaus, M, O’Brien, JK, Perovich, D, Ren,  
1594 J, Rex, M, Ribeiro, N, Rinke, A, Schaffer, J, Schuffenhauer, I, Schulz, K,  
1595 Shupe, MD, Shaw, W, Sokolov, V, Sommerfeld, A, Spreen, G, Stanton, T,  
1596 Stephens, M, Su, J, Sukhikh, N, Sundfjord, A, Thomisch, K, Tippenhauer,  
1597 S, Toole, JM, Vredenburg, M, Walter, M, Wang, H, Wang, L, Wang, Y,  
1598 Wendisch, M, Zhao, J, Zhou, M, Zhu, J, Laukert, G. 2022. Overview of the  
1599 MOSAiC expedition: Physical oceanography. *Elementa: Science of the An-  
1600 thropocene* **10**(1). doi:https://doi.org/10.1525/elementa.2021.00062.

- 1601 Randelhoff, A, Holding, J, Janout, M, Sejr, MK, Babin, M, Tremblay, JE,  
1602 Alkire, MB. 2020. Pan-Arctic Ocean Primary Production Constrained  
1603 by Turbulent Nitrate Fluxes. *Frontiers in Marine Science* **7**: 150. doi:  
1604 <https://doi.org/10.3389/fmars.2020.00150>.
- 1605 Rantanen, M, Karpechko, AY, Lipponen, A, Nordling, K, Hyvärinen, O, Ruos-  
1606 teenoja, K, Vihma, T, Laaksonen, A. 2022. The Arctic has warmed nearly  
1607 four times faster than the globe since 1979. *Communications Earth & Envi-*  
1608 *ronment* **3**(1): 168. doi:<https://doi.org/10.1038/s43247-022-00498-3>.
- 1609 Rex, M, Hoppmann, M, Tippenhauer, S, Rohardt, G. 2021a. Continuous thermos-  
1610 alinograph oceanography along RV POLARSTERN cruise track PS122/1.  
1611 PANGAEA. doi:<https://doi.org/10.1594/PANGAEA.930023>.
- 1612 Rex, M, Hoppmann, M, Tippenhauer, S, Rohardt, G. 2021b. Continuous thermos-  
1613 alinograph oceanography along RV POLARSTERN cruise track PS122/4.  
1614 PANGAEA. doi:<https://doi.org/10.1594/PANGAEA.930027>.
- 1615 Rex, M, Hoppmann, M, Tippenhauer, S, Rohardt, G. 2021c. Continuous thermos-  
1616 alinograph oceanography along RV POLARSTERN cruise track PS122/5.  
1617 PANGAEA. doi:<https://doi.org/10.1594/PANGAEA.930028>.
- 1618 Rippeth, TP, Lincoln, BJ, Lenn, YD, Green, JM, Sundfjord, A, Ba-  
1619 con, S. 2015. Tide-mediated warming of Arctic halocline by Atlantic  
1620 heat fluxes over rough topography. *Nature Geoscience* **8**(3): 191. doi:  
1621 <https://doi.org/10.1038/ngeo2350>.
- 1622 Rogge, A, Janout, M, Loginova, N, Trudnowska, E, Hörstmann, C, Wekerle,  
1623 C, Oziel, L, Schourup-Kristensen, V, Ruiz-Castillo, E, Schulz, K, et al.  
1624 2023. Carbon dioxide sink in the Arctic Ocean from cross-shelf trans-  
1625 port of dense Barents Sea water. *Nature Geoscience* **16**(1): 82–88. doi:  
1626 <https://doi.org/10.1038/s41561-022-01069-z>.
- 1627 Rudels, B. 2009. Arctic ocean circulation. Academic Press.
- 1628 Rudels, B. 2015. Arctic Ocean circulation, processes and water masses: A de-  
1629 scription of observations and ideas with focus on the period prior to the In-  
1630 ternational Polar Year 2007–2009. *Progress in Oceanography* **132**: 22–67.  
1631 doi:<https://doi.org/10.1016/j.pocean.2013.11.006>.
- 1632 Rudels, B, Hainbucher, D. 2020. On the formation and spreading of thermohaline  
1633 intrusions in the Arctic Ocean. *Geophysica* **55**(1-2): 23–59.
- 1634 Rudels, B, et al. 2012. Arctic Ocean circulation and variability-advection and ex-  
1635 ternal forcing encounter constraints and local processes. *Ocean Science* doi:  
1636 <https://doi.org/10.5194/os-8-261-2012>.
- 1637 Salganik, E, Katlein, C, Lange, BA, Matero, I, Lei, R, Fong, AA, Fons, SW,  
1638 Divine, D, Oggier, M, Castellani, G, et al. 2023a. Temporal evolution of

- 1639 under-ice meltwater layers and false bottoms and their impact on summer  
1640 Arctic sea ice mass balance. *Elementa: Science of the Anthropocene* **11**(1).  
1641 doi:<https://doi.org/10.1525/elementa.2022.00035>.
- 1642 Salganik, E, Lange, BA, Katlein, C, Matero, I, Anhaus, P, Muilwijk, M, Høyland,  
1643 KV, Granskog, MA. 2023b. Observations of preferential summer melt of  
1644 Arctic sea-ice ridge keels from repeated multibeam sonar surveys. *The*  
1645 *Cryosphere* **17**(11): 4873–4887. doi:10.5194/tc-17-4873-2023.
- 1646 Schauer, U, Muench, RD, Rudels, B, Timokhov, L. 1997. Impact of east-  
1647 ern Arctic shelf waters on the Nansen Basin intermediate layers.  
1648 *Journal of Geophysical Research: Oceans* **102**(C2): 3371–3382. doi:  
1649 <https://doi.org/10.1029/96JC03366>.
- 1650 Schmale, J, Zieger, P, Ekman, AM. 2021. Aerosols in current and fu-  
1651 ture Arctic climate. *Nature Climate Change* **11**(2): 95–105. doi:  
1652 <https://doi.org/10.1038/s41558-020-00969-5>.
- 1653 Schmidtko, S, Johnson, GC, Lyman, JM. 2013. MIMOC: A global  
1654 monthly isopycnal upper-ocean climatology with mixed layers. *Jour-  
1655 nal of Geophysical Research: Oceans* **118**(4). ISSN 21699291. doi:  
1656 <https://doi.org/10.1002/jgrc.20122>.
- 1657 Schulz, K, Janout, M, Lenn, YD, Ruiz-Castillo, E, Polyakov, I, Mohrholz, V,  
1658 Tippenhauer, S, Reeve, K, Hölemann, J, Rabe, B, Vredenburg, M. 2021.  
1659 On the along-slope heat loss of the Boundary Current in the Eastern Arctic  
1660 Ocean. *Journal of Geophysical Research: Oceans* **126**(2): e2020JC016375.  
1661 doi:<https://doi.org/10.1029/2020JC016375>.
- 1662 Schulz, K, Kadko, D, Mohrholz, V, Stephens, M, Fer, I. 2023a. Winter verti-  
1663 cal diffusion rates in the Arctic Ocean, estimated from <sup>7</sup>Be measurements  
1664 and dissipation rate profiles. *Journal of Geophysical Research: Oceans* pp.  
1665 e2022JC019197. doi:<https://doi.org/10.1029/2022JC019197>.
- 1666 Schulz, K, Koenig, Z, Muilwijk, M. 2023b. The Eurasian Arctic Ocean along  
1667 the MOSAiC drift (2019-2020): Core hydrographic parameters. Arctic Data  
1668 Center. doi:doi:10.18739/A21J9790B.
- 1669 Schulz, K, Lincoln, B, Povazhnyy, V, Rippeth, T, Lenn, YD, Janout, M, Alkire, M,  
1670 Scannell, B, Torres-Valdés, S. 2022a. Increasing nutrient fluxes and mixing  
1671 regime changes in the eastern Arctic Ocean. *Geophysical Research Letters*  
1672 pp. e2021GL096152. doi:<https://doi.org/10.1029/2021GL096152>.
- 1673 Schulz, K, Mohrholz, V, Fer, I, Janout, M, Hoppmann, M, Schaffer, J, Koenig,  
1674 Z. 2022b. A full year of turbulence measurements from a drift cam-  
1675 paign in the Arctic Ocean 2019—2020. *Scientific Data* **9**(472). doi:  
1676 <https://doi.org/10.1038/s41597-022-01574-1>.

- 1677 Schulz, K, Mohrholz, V, Fer, I, Janout, MA, Hoppmann, M, Schaffer, J, Koenig,  
1678 Z, Rabe, B, Heuzé, C, Regnery, J, Allerholt, J, Fang, YC, He, H, Kanzow,  
1679 T, Karam, S, Kuznetsov, I, Kong, B, Liu, H, Muilwijk, M, Schuffenhauer, I,  
1680 Sukhikh, N, Sundfjord, A, Tippenhauer, S. 2023c. Turbulent microstructure  
1681 profile (MSS) measurements from the MOSAiC drift, Arctic Ocean, version  
1682 2. PANGAEA. doi:<https://doi.pangaea.de/10.1594/PANGAEA.961798>.
- 1683 Schuster, U, McKinley, GA, Bates, N, Chevallier, F, Doney, SC, Fay, AR,  
1684 González-Dávila, M, Gruber, N, Jones, S, Krijnen, J, et al. 2013. An assess-  
1685 ment of the Atlantic and Arctic sea–air CO<sub>2</sub> fluxes, 1990–2009. *Biogeo-*  
1686 *sciences* **10**(1): 607–627. doi:<https://doi.org/10.5194/bg-10-607-2013>.
- 1687 Shaw, WJ, Stanton, TP. 2014. Vertical diffusivity of the Western Arctic Ocean  
1688 halocline. *Journal of Geophysical Research: Oceans* **119**(8): 5017–5038.  
1689 doi:<https://doi.org/10.1002/2013JC009598>.
- 1690 Shibley, NC, Timmermans, ML, Carpenter, JR, Toole, JM. 2017. Spa-  
1691 tial variability of the Arctic Ocean’s double-diffusive staircase.  
1692 *Journal of Geophysical Research: Oceans* **122**(2): 980–994. doi:  
1693 <https://doi.org/10.1002/2016JC012419>.
- 1694 Shupe, MD, Rex, M, Blomquist, B, Persson, POG, Schmale, J, Uttal, T, Al-  
1695 thausen, D, Angot, H, Archer, S, Bariteau, L, et al. 2022. Overview of  
1696 the MOSAiC expedition: Atmosphere. University of California Press. doi:  
1697 <https://doi.org/10.1525/elementa.2021.00060>.
- 1698 Sirevaag, A, Fer, I. 2012. Vertical heat transfer in the Arctic Ocean: The role of  
1699 double-diffusive mixing. *Journal of Geophysical Research: Oceans* **117**(C7).  
1700 doi:<https://doi.org/10.1029/2012JC007910>.
- 1701 Skogseth, R, McPhee, MG, Nilsen, F, Smedsrud, LH. 2013. Creation and  
1702 tidal advection of a cold salinity front in Storfjorden: 1. Polynya dynam-  
1703 ics. *Journal of Geophysical Research: Oceans* **118**(7): 3278–3291. doi:  
1704 <https://doi.org/10.1002/jgrc.20231>.
- 1705 Smedsrud, LH, Esau, I, Ingvaldsen, RB, Eldevik, T, Haugan, PM, Li, C, Lien,  
1706 VS, Olsen, A, Omar, AM, Otterå, OH, et al. 2013. The role of the Barents  
1707 Sea in the Arctic climate system. *Reviews of Geophysics* **51**(3): 415–449.  
1708 doi:<https://doi.org/10.1002/rog.20017>.
- 1709 Smethie Jr, W, Chipman, D, Swift, J, Koltermann, K. 1988. Chlorofluoromethanes  
1710 in the Arctic Mediterranean seas: evidence for formation of bottom water  
1711 in the Eurasian Basin and deep-water exchange through Fram Strait. *Deep*  
1712 *Sea Research Part A Oceanographic Research Papers* **35**(3): 347–369. doi:  
1713 [https://doi.org/10.1016/0198-0149\(88\)90015-5](https://doi.org/10.1016/0198-0149(88)90015-5).
- 1714 Smith, MM, Angot, H, Chamberlain, EJ, Droste, ES, Karam, S, Muilwijk, M,



- 1715 Webb, AL, Archer, SD, Beck, I, Blomquist, BW, Bowman, J, Boyer, M, Boz-  
1716 zato, D, Chierici, M, Creamean, J, D'Angelo, A, Delille, B, Fer, I, Fong, AA,  
1717 Fransson, A, Fuchs, N, Gardner, J, Granskog, MA, Hoppe, CJM, Hoppema,  
1718 M, Hoppmann, M, Mock, T, Muller, S, Müller, O, Nicolaus, M, Nomura,  
1719 D, Petäjä, T, Salganik, E, Schmale, J, Schmidt, K, Schulz, KM, Shupe, MD,  
1720 Stefels, J, Thielke, L, Tippenhauer, S, Ulfsbo, A, van Leeuwe, M, Webster,  
1721 M, Yoshimura, M, Zhan, L. 2023. Thin and transient meltwater layers and  
1722 false bottoms in the Arctic sea ice pack—Recent insights on these histori-  
1723 cally overlooked features. *Elementa: Science of the Anthropocene* **11**(1). doi:  
1724 10.1525/elementa.2023.00025.
- 1725 Smith, MM, von Albedyll, L, Raphael, IA, Lange, BA, Matero, I, Salganik, E,  
1726 Webster, MA, Granskog, MA, Fong, A, Lei, R, Light, B. 2022. Quantifying  
1727 false bottoms and under-ice meltwater layers beneath Arctic summer sea ice  
1728 with fine-scale observations. *Elementa: Science of the Anthropocene* **10**(1):  
1729 000116. ISSN 2325-1026. doi:10.1525/elementa.2021.000116.
- 1730 Snoeijs-Leijonmalm, P, Flores, H, Sakinan, S, Hildebrandt, N, Svenson, A, Castel-  
1731 lani, G, Vane, K, Mark, FC, Heuzé, C, Tippenhauer, S, et al. 2022. Unex-  
1732 pected fish and squid in the central Arctic deep scattering layer. *Science ad-*  
1733 *vances* **8**(7): eabj7536. doi:https://doi.org/10.1126/sciadv.abj7536.
- 1734 Somavilla, R, Schauer, U, Budéus, G. 2013. Increasing amount of Arctic Ocean  
1735 deep waters in the Greenland Sea. *Geophysical Research Letters* **40**(16):  
1736 4361–4366. doi:https://doi.org/10.1002/grl.50775.
- 1737 Son, E, Kawaguchi, Y, Cole, S, Toole, J, Ha, H. 2022. Assessment  
1738 of Turbulent Mixing Associated With Eddy-Wave Coupling Based  
1739 on Autonomous Observations From the Arctic Canada Basin. *Journal of Geophysical Research: Oceans* **127**(9): e2022JC018489. doi:  
1740 https://doi.org/10.1029/2022JC018489.
- 1742 Stedmon, CA, Amon, RMW, Bauch, D, Bracher, A, Gonçalves-Araujo, R, Hopp-  
1743 mann, M, Krishfield, RA, Laney, S, Rabe, B, Reader, HE, Granskog, MA.  
1744 2021. Intercalibrated dataset of in situ dissolved organic matter fluorescence  
1745 collected using Ice Tethered Profilers in the Central Arctic (2011-2016).  
1746 PANGAEA. doi:10.1594/PANGAEA.934370.
- 1747 Stedmon, CA, Amon, RMW, Bauch, D, Bracher, A, Gonçalves-Araujo, R,  
1748 Hoppmann, M, Krishfield, R, Laney, S, Rabe, B, Reader, H, Granskog,  
1749 MA. 2021. Insights Into Water Mass Origins in the Central Arc-  
1750 tic Ocean From In-Situ Dissolved Organic Matter Fluorescence. *Journal of Geophysical Research: Oceans* **126**(7): e2021JC017407. doi:  
1751 https://doi.org/10.1029/2021JC017407.  
1752

- 1753 Steele, M, Boyd, T. 1998. Retreat of the cold halocline layer in the Arctic  
1754 Ocean. *Journal of Geophysical Research: Oceans* **103**(C5): 10419–10435.  
1755 doi:<https://doi.org/10.1029/98JC00580>.
- 1756 Steele, M, Morison, J, Ermold, W, Rigor, I, Ortmeyer, M, Shimada,  
1757 K. 2004. Circulation of summer Pacific halocline water in the Ar-  
1758 ctic Ocean. *Journal of Geophysical Research: Oceans* **109**(C2). doi:  
1759 <https://doi.org/10.1029/2003JC002009>.
- 1760 Steele, M, Morley, R, Ermold, W. 2001. PHC3 Updated from: A global  
1761 ocean hydrography with a high quality Arctic Ocean. *Journal of Cli-*  
1762 *mate* **14**(9): 2079–2087. ISSN 1520-0442. doi:[https://doi.org/10.1175/1520-](https://doi.org/10.1175/1520-0442(2001)014;2079:PAGOHW;2.0.CO;2)  
1763 [0442\(2001\)014;2079:PAGOHW;2.0.CO;2](https://doi.org/10.1175/1520-0442(2001)014;2079:PAGOHW;2.0.CO;2).
- 1764 Stroeve, J, Serreze, M, Drobot, S, Gearheard, S, Holland, M, Maslanik,  
1765 J, Meier, W, Scambos, T. 2008. Arctic sea ice extent plummets in  
1766 2007. *Eos, Transactions American Geophysical Union* **89**(2): 13–14. doi:  
1767 <https://doi.org/10.1029/2008EO020001>.
- 1768 Takahashi, T, Sutherland, SC, Wanninkhof, R, Sweeney, C, Feely, RA,  
1769 Chipman, DW, Hales, B, Friederich, G, Chavez, F, Sabine, C, et al.  
1770 2009. Climatological mean and decadal change in surface ocean pCO<sub>2</sub>,  
1771 and net sea–air CO<sub>2</sub> flux over the global oceans. *Deep Sea Re-*  
1772 *search Part II: Topical Studies in Oceanography* **56**(8-10): 554–577. doi:  
1773 <https://doi.org/10.1016/j.dsr2.2008.12.009>.
- 1774 Tanhua, T, Jones, EP, Jeansson, E, Jutterström, S, Smethie Jr, WM, Wallace, DW,  
1775 Anderson, LG. 2009. Ventilation of the Arctic Ocean: Mean ages and inven-  
1776 tories of anthropogenic CO<sub>2</sub> and CFC-11. *Journal of Geophysical Research:*  
1777 *Oceans* **114**(C1). doi:<https://doi.org/10.1029/2008JC004868>.
- 1778 Terhaar, J, Lauerwald, R, Regnier, P, Gruber, N, Bopp, L. 2021. Around  
1779 one third of current Arctic Ocean primary production sustained by  
1780 rivers and coastal erosion. *Nature Communications* **12**(1): 169. doi:  
1781 <https://doi.org/10.1038/s41467-020-20470-z>.
- 1782 Timmermans, ML, Marshall, J. 2020. Understanding Arctic Ocean circu-  
1783 lation: A review of ocean dynamics in a changing climate. *Jour-*  
1784 *nal of Geophysical Research: Oceans* **125**(4): e2018JC014378. doi:  
1785 <https://doi.org/10.1029/2018JC014378>.
- 1786 Timmermans, ML, Toole, JM. 2023. The Arctic Ocean’s Beaufort Gyre. *Annual*  
1787 *Review of Marine Science* **15**: 223–248. doi:[https://doi.org/10.1146/annurev-](https://doi.org/10.1146/annurev-marine-032122-012034)  
1788 [marine-032122-012034](https://doi.org/10.1146/annurev-marine-032122-012034).
- 1789 Tippenhauer, S, Janout, M, Chouksey, M, Torres-Valdes, S, Fong, A, Wulff,  
1790 T. 2021. Substantial sub-surface chlorophyll patch sustained by ver-

- 1791 tical nutrient fluxes in Fram Strait observed with an autonomous  
1792 underwater vehicle. *Frontiers in Marine Science* **8**: 605225. doi:  
1793 <https://doi.org/10.3389/fmars.2021.605225>.
- 1794 Tippenhauer, S, Vredenburg, M, Heuzé, C, Ulfsbo, A, Rabe, B, Granskog,  
1795 MA, Allerholt, J, Balmonte, JP, Campbell, RG, Castellani, G, Chamber-  
1796 lain, E, Creamean, J, D'Angelo, A, Dietrich, U, Droste, E, Eggers, L,  
1797 Fang, YC, Fong, AA, Gardner, J, Graupner, R, Grosse, J, He, H, Hilde-  
1798 brandt, N, Hoppe, CJM, Hoppmann, M, Kanzow, T, Karam, S, Koenig,  
1799 Z, Kong, B, Kuhlmeier, D, Kuznetsov, I, Lan, M, Liu, H, Mallet, M,  
1800 Mohrholz, V, Muilwijk, M, Müller, O, Olsen, LM, Rember, R, Ren, J,  
1801 Sakinan, S, Schaffer, J, Schmidt, K, Schuffenhauer, I, Schulz, K, Shoemaker, K, Spahic, S, Sukhikh, N, Svenson, A, Torres-Valdés, S, Torstensson, A, Wischnewski, L, Zhuang, Y. 2023a. Physical oceanography based on Ocean City CTD during POLARSTERN cruise PS122. PANGAEA. doi:  
1802 <https://doi.pangaea.de/10.1594/PANGAEA.959964>.
- 1806 Tippenhauer, S, Vredenburg, M, Heuzé, C, Ulfsbo, A, Rabe, B, Granskog, MA,  
1807 Allerholt, J, Balmonte, JP, Campbell, RG, Castellani, G, Chamberlain, E,  
1808 Creamean, J, D'Angelo, A, Dietrich, U, Droste, E, Eggers, L, Fang, YC,  
1809 Fong, AA, Gardner, J, Graupner, R, Grosse, J, He, H, Hildebrandt, N, Hoppe,  
1810 CJM, Hoppmann, M, Kanzow, T, Karam, S, Koenig, Z, Kong, B, Kuhlmeier,  
1811 D, Kuznetsov, I, Lan, M, Liu, H, Mallet, M, Mohrholz, V, Muilwijk, M,  
1812 Müller, O, Olsen, LM, Rember, R, Ren, J, Sakinan, S, Schaffer, J, Schmidt,  
1813 K, Schuffenhauer, I, Schulz, K, Shoemaker, K, Spahic, S, Sukhikh, N, Svenson, A, Torres-Valdés, S, Torstensson, A, Wischnewski, L, Zhuang, Y. 2023b. Physical oceanography based on ship CTD during POLARSTERN cruise PS122. PANGAEA. doi:  
1814 <https://doi.pangaea.de/10.1594/PANGAEA.959963>.
- 1817 Tippenhauer, S, Vredenburg, M, Heuzé, C, Ulfsbo, A, Rabe, B, Granskog,  
1818 MA, Allerholt, J, Balmonte, JP, Campbell, RG, Castellani, G, Chamber-  
1819 lain, E, Creamean, J, D'Angelo, A, Dietrich, U, Droste, E, Eggers, L,  
1820 Fang, YC, Fong, AA, Gardner, J, Graupner, R, Grosse, J, He, H, Hilde-  
1821 brandt, N, Hoppe, CJM, Hoppmann, M, Kanzow, T, Karam, S, Koenig, Z,  
1822 Kong, B, Kuhlmeier, D, Kuznetsov, I, Lan, M, Liu, H, Mallet, M, Mohrholz,  
1823 V, Muilwijk, M, Müller, O, Olsen, LM, Rember, R, Ren, J, Sakinan,  
1824 S, Schaffer, J, Schmidt, K, Schuffenhauer, I, Schulz, K, Shoemaker, K,  
1825 Spahic, S, Sukhikh, N, Svenson, A, Torres-Valdés, S, Torstensson, A, Wischnewski, L, Zhuang, Y. 2023c. Physical oceanography water bottle samples based on ship CTD during POLARSTERN cruise PS122. PANGAEA. doi:  
1826 <https://doi.pangaea.de/10.1594/PANGAEA.959965>.

- 1829 Tippenhauer, S, Vredenburg, M, Heuzé, C, Ulfsbo, A, Rabe, B, Granskog, MA,  
1830 Allerholt, J, Balmonte, JP, Campbell, RG, Castellani, G, Chamberlain, E,  
1831 Creamean, J, D'Angelo, A, Dietrich, U, Droste, E, Eggers, L, Fang, YC,  
1832 Fong, AA, Gardner, J, Graupner, R, Grosse, J, He, H, Hildebrandt, N,  
1833 Hoppe, CJM, Hoppmann, M, Kanzow, T, Karam, S, Koenig, Z, Kong, B,  
1834 Kuhlmeier, D, Kuznetsov, I, Lan, M, Liu, H, Mallet, M, Mohrholz, V, Muil-  
1835 wijk, M, Müller, O, Olsen, LM, Rember, R, Ren, J, Sakinan, S, Schaf-  
1836 fer, J, Schmidt, K, Schuffenhauer, I, Schulz, K, Shoemaker, K, Spahic, S,  
1837 Sukhikh, N, Svenson, A, Torres-Valdés, S, Torstensson, A, Wischniewski,  
1838 L, Zhuang, Y. 2023d. Physical oceanography water bottle samples based  
1839 on Ocean City CTD during POLARSTERN cruise PS122. PANGAEA. doi:  
1840 <https://doi.pangaea.de/10.1594/PANGAEA.959966>.
- 1841 Toole, JM, Krishfield, R. 2016. Woods Hole Oceanographic Institution Ice-  
1842 Tethered Profiler Program. Ice-Tethered Profiler observations: Vertical pro-  
1843 files of temperature, salinity, oxygen, and ocean velocity from an Ice-  
1844 Tethered Profiler buoy system. [ITP94, ITP111, Accessed March 13,  
1845 2023]. NOAA National Centers for Environmental Information. doi:  
1846 <https://doi.org/10.7289/v5mw2f7x>.
- 1847 Toole, JM, Krishfield, RA, Timmermans, ML, Proshutinsky, A. 2011. The ice-  
1848 tethered profiler: Argo of the Arctic. *Oceanography* **24**(3): 126–135. doi:  
1849 <https://doi.org/10.5670/oceanog.2011.64>.
- 1850 Torres-Valdés, S, Tsubouchi, T, Bacon, S, Naveira-Garabato, AC, Sanders, R,  
1851 McLaughlin, FA, Petrie, B, Kattner, G, Azetsu-Scott, K, Whitlege, TE.  
1852 2013. Export of nutrients from the Arctic Ocean. *Journal of Geophysical Re-  
1853 search: Oceans* **118**(4): 1625–1644. doi:<https://doi.org/10.1002/jgrc.20063>.
- 1854 von Appen, WJ, Baumann, TM, Janout, M, Koldunov, N, Lenn, YD, Pickart,  
1855 RS, Scott, RB, Wang, Q. 2022. Eddies and the distribution of eddy ki-  
1856 netic energy in the Arctic Ocean. *Oceanography* **35**(3/4): 42–51. doi:  
1857 <https://www.jstor.org/stable/27182695>.
- 1858 von Appen, WJ, Schauer, U, Somavilla, R, Bauerfeind, E, Beszczynska-Möller,  
1859 A. 2015. Exchange of warming deep waters across Fram Strait. *Deep  
1860 Sea Research Part I: Oceanographic Research Papers* **103**: 86–100. doi:  
1861 <https://doi.org/10.1016/j.dsr.2015.06.003>.
- 1862 Wang, Q, Shu, Q, Bozec, A, Chassignet, EP, Fogli, PG, Fox-Kemper, B, Hogg,  
1863 AM, Iovino, D, Kiss, AE, Koldunov, N, Le Sommer, J, Li, Y, Lin, P, Liu,  
1864 H, Polyakov, I, Scholz, P, Sidorenko, D, Wang, S, Xu, X. 2023. Impact of  
1865 high resolution on Arctic Ocean simulations in Ocean Model Intercompar-  
1866 ison Project phase 2 (OMIP-2). *Geoscientific Model Development Discus-*

- 1867 *sions* **2023**: 1–46. doi:<https://doi.org/10.5194/gmd-2023-123>.
- 1868 Webster, MA, Holland, M, Wright, NC, Hendricks, S, Hutter, N, Itkin, P, Light,  
1869 B, Linhardt, F, Perovich, DK, Raphael, IA, et al. 2022. Spatiotemporal  
1870 evolution of melt ponds on Arctic sea ice: MOSAiC observations and  
1871 model results. *Elementa Science of the Anthropocene* **10**(1): 000072. doi:  
1872 <https://doi.org/10.1525/elementa.2021.000072>.
- 1873 Zhao, M, Timmermans, ML, Cole, S, Krishfield, R, Proshutinsky, A, Toole,  
1874 J. 2014. Characterizing the eddy field in the Arctic Ocean halocline.  
1875 *Journal of Geophysical Research: Oceans* **119**(12): 8800–8817. doi:  
1876 <https://doi.org/10.1002/2014JC010488>.
- 1877 Zweng, M, Reagan, J, Seidov, D, Boyer, T, Locarnini, R, Garcia, H, Mishonov,  
1878 A, Baranova, O, Weathers, K, Paver, C, Smolyar, I. 2018. *World Ocean Atlas*  
1879 *2018, Volume 2: Salinity*. A. Mishonov Technical Ed.; NOAA Atlas NESDIS  
1880 82.